

Two-dimensional spectroscopy of bosonic collective excitations in disordered many-body systems

Alex Gómez Salvador,^{1,*} Ivan Morera,^{1,*} Marios H. Michael,² Pavel E. Dolgirev,³
Danica Pavicevic,² Albert Liu,⁴ Andrea Cavalleri,^{2,5} and Eugene Demler¹

¹*Institute for Theoretical Physics, ETH Zurich, 8093 Zurich, Switzerland.*

²*Max Planck Institute for the Structure and Dynamics of Matter, Luruper Chaussee 149, 22761 Hamburg, Germany.*

³*Department of Physics, Harvard University, Cambridge, Massachusetts 02138, USA.*

⁴*Condensed Matter Physics and Materials Science Division, Brookhaven National Laboratory, Upton, New York 11973, USA.*

⁵*Clarendon Laboratory, University of Oxford, Parks Road, Oxford OX1 3PU, UK.*

(Dated: January 29, 2025)

We present a novel theoretical approach for computing and analyzing two-dimensional spectroscopy of bosonic collective excitations in disordered many-body systems. Specifically, we employ the Keldysh formalism to derive the nonlinear response and obtain two-dimensional spectroscopy maps with particular emphasis on the rephasing sector, which allows to disentangle different sources of broadening. Our many-body approach successfully distinguishes elastic and inelastic scattering mechanisms contributing to the excitation linewidth. Additionally, using a non-perturbative conserving approach, we demonstrate that the echo peak exhibits a universal asymmetric shape in the sole presence of static disorder, a feature that remains robust against quantum fluctuations. This is in stark contrast to the standard theory based on isolated two-level systems, which fails to account for the dispersive nature of excitations and the interactions between different momentum components.

I. INTRODUCTION

Linear response theory underlies most of the traditional experimental techniques in quantum many-body physics. In such experiments, results can be interpreted from the perspective of two-point correlation functions of appropriate operators. In the case of electron systems, paradigmatic examples include density operators for X-ray scattering [1, 2], current operators for optical spectroscopy [3] and transport [4, 5], and electron creation and annihilation operators for STM [6] and ARPES [7] experiments. Collective excitations manifest themselves as peaks in the response functions and provide clear signatures of underlying many-body states. Investigations of collective modes using linear response probes have been ubiquitous in physics, chemistry, biology, and material science. However, despite their immense accomplishments, these techniques also present certain shortcomings. For instance, understanding the origin of the excitation broadening can be challenging since different mechanisms often result in similar lineshapes. The extension of linear response measurements to the nonlinear regime, and the consequent access to higher-order correlators, has opened the door to circumvent some of these limitations. Of special relevance are the accomplishments of nuclear magnetic resonance (NMR) [8–14] and its optical analogs termed multidimensional coherent spectroscopies (MDCS) [15–22]. For instance, these approaches have been employed to identify different interaction mechanisms between excitations [23–25], resolve energy transfer pathways [26–29], classify bound states [30–

32], and disentangle homogeneous and inhomogeneous broadening [33–35].

In condensed matter systems, the characteristic low-energy excitations typically lie in the terahertz frequency (THz) range, including Josephson plasmons in high temperature superconductors [36–41], magnons [42–44], and cyclotron orbits in 2D electron gas [45, 46], among many others. Historically, the well-known THz gap [47] has hindered the use of nonlinear probes in studying said low-energy excitations. However, the recent progress in terahertz technology [48, 49] has led to the development of a terahertz analogue of multidimensional optical spectroscopies, known as two-dimensional terahertz spectroscopy (2DTS) [50–61]. In recent years, this technique has been applied to a wide-range of condensed matter systems, including superconductors [58, 62–67], correlated metals [68] and insulators [69], ferroics [70–74], topological materials [75–77], and spin liquids [78–80] and ices [81].

Similarly to MDCS, 2DTS is poised to be a promising technique to disentangle different sources of broadening in a correlated many-body system. However, the applicability of the standard interpretation in terms of homogeneous and inhomogeneous broadening in a system of isolated two-level systems (ITLS) becomes questionable when studying collective modes. This is particularly relevant when studying the influence of randomness and spatial inhomogeneity, since the effects of disorder strongly depend on the nature of excitations. In the case of dispersive collective excitations, elastic scattering due to a disorder potential changes their momentum but not energy. In the standard ITLS treatment, this would be misinterpreted as homogeneous broadening, despite the collective mode having an infinite lifetime in the absence of disorder.

* These authors contributed equally to this work.

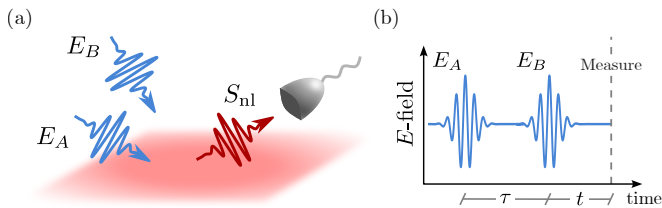


FIG. 1. (a) Cartoon of the standard two-dimensional terahertz spectroscopy protocol. External perturbations E_A and E_B are sent with a relative time delay τ (b). After a waiting t with respect to the arrival of the second pulse, the measurement of the resulting nonlinear signal S_{nl} is performed.

This paper provides a new theoretical framework for analyzing 2DTS for collective excitations in the presence of static spatial disorder. Employing a conserving field-theoretical approach in the Keldysh formalism we compute the third-order nonlinear response of a many-body system and obtain the characteristic asymmetric (almond-like) echo peak signature in the 2DTS protocol. In particular, we demonstrate the non-perturbative nature of the rephasing physics and the necessity to consider the infinite series of non-crossing disorder diagrams. In the sole presence of static disorder, we find a universal echo peak asymmetry independent of the disorder strength and robust against quantum fluctuations. This is in stark contrast to the ITLS scenario where the echo becomes more asymmetric as disorder increases. Finally, when both elastic and inelastic scattering are present, we demonstrate how two-dimensional spectroscopy in collective excitations is capable of disentangling the two broadening mechanisms.

The rest of the paper is organized as follows. In Sec. II, we introduce the 2DTS protocol and provide an intuitive discussion of the signatures of disorder in the 2D maps. In Sec. III, we describe our theoretical approach to compute the nonlinear 2D maps within the Keldysh path integral formalism and provide a general equation for the third-order susceptibility in terms of the linear susceptibility and the “dressed” vertex. In Sec. IV, we outline a conserving calculation of the third-order susceptibility and the associated 2D map for a system without disorder. Then, in Sec. V, we detail the calculations of the 2D map considering static disorder. In Sec. VI, we discuss the signatures of the 2D map when both elastic and inelastic scattering are considered simultaneously. Finally, in Sec. VII, we present our conclusions and outlook.

II. ECHO PEAK IN MANY-BODY SYSTEMS: ITLS AND COLLECTIVE EXCITATIONS

To set notations for subsequent discussion of disordered quantum many-body systems, we first describe the standard 2DTS protocol and introduce the two-dimensional (2D) map. Then, we provide a qualitative discussion on the signatures of disorder in the 2D map

for ITLS and collective excitations, and motivate the necessity for a reformulation of the interpretation of the disorder effects.

The standard 2DTS protocol can be summarized as follows: An external perturbation consisting of two identical excitation pulses, denoted E_A and E_B , separated by a time delay $\tau > 0$, is sent towards the sample. After the arrival of the second pulse, the system is left to evolve unperturbed for time $t > 0$, after which the measurement is performed to obtain the signal $S(\tau, t)$, see Fig. 1. In this type of protocols, both the linear contributions in E_A or E_B , and the self-nonlinearities proportional to E_A^3 and E_B^3 are usually filtered out experimentally. This leaves behind a purely nonlinear signal $S_{nl}(\tau, t)$ with terms proportional to $E_A^2 E_B$ (A) and $E_A E_B^2$ (B). Assuming the pulses to be perfect Dirac delta functions, the $E_A^2 E_B$ signal can be obtained from the third-order nonlinear response $\chi^{(3)}$ via

$$S_{nl}^A(t, \tau) = 3 \int \prod_{i=1}^3 \frac{d\omega_i}{2\pi} \chi^{(3)}(\omega_3, \omega_2, \omega_1) e^{-i(\omega_1 + \omega_2)\tau} e^{-i\bar{\omega}t}, \quad (1)$$

and similarly for the $E_A E_B^2$ signal:

$$S_{nl}^B(t, \tau) = 3 \int \prod_{i=1}^3 \frac{d\omega_i}{2\pi} \chi^{(3)}(\omega_3, \omega_2, \omega_1) e^{-i\omega_1\tau} e^{-i\bar{\omega}t}, \quad (2)$$

where $\bar{\omega} = \omega_1 + \omega_2 + \omega_3$. The 2D map is subsequently obtained upon performing a double Fourier transform with respect to t and τ restricted to $t > 0$ and $\tau > 0$. Of special interest in multidimensional spectroscopy is the so-called echo peak, or rephasing peak, a nonlinear signal contained in the $E_A E_B^2$ contribution of the 2D map, analogous in nature to the spin echo [82]. This peak has been successfully employed in NMR and MDCS to disentangle and quantify the presence and strength of homogeneous and inhomogeneous broadening [83]. We now discuss and contrast the echo peaks for ITLS and collective excitations

First, consider an ensemble of non-interacting ITLS spatially distributed such that their resonance frequency depends on their position, see Fig. 2(a). In the simplest theoretical treatment, one introduces the linewidth γ , characterizing the T_1 and T_2 processes (homogeneous broadening), and assumes a Gaussian distribution for the resonance frequencies with mean ω_0 and variance σ (inhomogeneous broadening). Under these assumptions, the time-domain echo nonlinearity in a 2-pulse protocol can be obtained exactly:

$$S(\tau, t) \sim \theta(\tau)\theta(t) e^{-i\omega_0(t-\tau)} e^{-\gamma(t+\tau)} e^{-\sigma^2(t-\tau)^2/2}. \quad (3)$$

The success of two-dimensional spectroscopy in disentangling homogeneous and inhomogeneous broadening is due to the rephasing nature of the echo peak, which exhibits a distinct time-dependence on the terms proportional to γ and σ . This distinct time-dependence results not only in a characteristic almond-like shape for the echo peak,

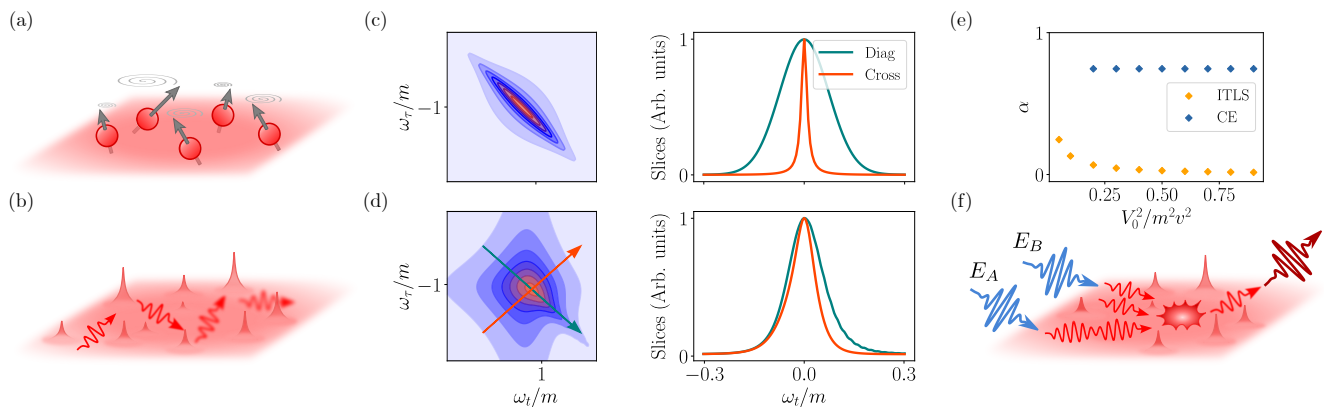


FIG. 2. (a)-(b) Cartoon of the effects of disorder on ITLS and collective excitations. In (a) an ensemble of two-level systems (spin precession) have a transition energy that depends on their position in space. Their collective signal presents a damping due to their intrinsically different oscillation frequencies. In (b) a collective excitation undergoes elastic scattering events due to the presence of disorder in the sample and becomes less well-defined after successive collisions. This series of scattering events results in a finite lifetime for the excitation. (c)-(d) Echo peak and slices along the diagonal (teal) and cross-diagonal (orange) of the echo peak for ITLS and collective excitations. In the sole presence of static disorder, the echo peak for ITLS (c) is strongly asymmetric with a cut along the cross-diagonal becoming infinitely sharp; for collective excitations (d) the asymmetry is less pronounced and the cut along the cross-diagonal presents a finite width. Note that for the sake of visualisation, we have included a finite small damping to the ITLS echo peak of $\eta/m = 0.01$, since otherwise, it would be infinitely sharp along the cross diagonal. (e) The striking differences in the signatures of the echo peak between ITLS and collective excitations (CE) can be efficiently captured by the ratio of full-width at half maximum of the two-diagonal cuts α . Furthermore, as we demonstrate in Sec. V, for collective excitations this ratio exhibits a robust value of $\alpha \approx 0.75$ within our approximation and in two spatial dimensions. (f) Schematic of the four-wave mixing process corresponding to the $E_A E_B^2$ sector in the 2DTS protocol in the presence of disorder.

but also enables a simultaneous fitting procedure for γ and σ based on two orthogonal diagonal cuts of the echo peak along $\omega_t \pm \omega_\tau$ [83], see Fig. 2(a) and (c).

Consider now a many-body system in the absence of disorder, when collective modes are infinitely long lived. When the system is driven by light, excitations are created or annihilated with zero momentum, causing them to oscillate at the mass (resonance) energy without any damping. However, if the medium is disordered, for example, due to the presence of static impurities, elastic scattering events will result in a finite lifetime leading to broad peaks in the 2D map; see Fig. 2(b) and (d). It is useful to contrast collective mode eigenstates in the presence of static disorder with propagators at specific momenta. While the former have well defined energies and infinite lifetimes (in the absence of interactions between modes), the latter have finite broadening, corresponding to finite lifetimes, and described mathematically by the self-energies of individual excitations Σ . We note, however, that when analyzing the nonlinear response of collective excitations, we need to go beyond the analysis of single particle lifetimes and take into account correlations that develop between different momentum components of the photoexcited collective modes. In the language of field theory, this means that we need to include "vertex corrections" (see sections IV and beyond for details).

We now contrast the physical picture of disorder induced excitation lifetimes for dispersive collective modes and ITLS. In the latter case, the different modes are, at

least within standard theoretical treatments, completely uncorrelated, and thus static disorder does not affect the intrinsic lifetime of each individual mode. However, the correlations present in the quantum many-body system do not allow for a separation between homogeneous and inhomogeneous broadening, since as we have established static disorder alone will result in a finite excitation lifetime. An interpretation based on such a separation can therefore lead to misleading conclusions. As we show in this paper, distinguishing between elastic and inelastic scattering events provides a more suitable separation of broadening mechanisms. These striking differences can be efficiently captured by the ratio of the full-width at half maximum of the diagonal cuts of the 2D map α , see Fig. 2(e). The ratio α decreases with the disorder strength for ITLS, whereas for collective excitations, this ratio exhibits a robust value of $\alpha \approx 0.75$. We demonstrate that this is a universal property of many-body systems with a bosonic collective mode and small quantum fluctuations, see Sec. V.

Having established the breakdown of the separation between homogeneous and inhomogeneous broadening, we now address the rephasing nature of the echo peak in a many-body system. In the simplest scenario, the essence of the echo peak and its characteristic almond shape relies on the system evolving with the same frequency during time delays τ and t . If this is to originate from scattering events, then these scatterings must correlate the excitations present during τ and t , causing them to explore

states with the same energy. These correlated scattering events between different excitations correspond to a four-wave mixing process which contains vertex corrections Γ , i.e. two particle corrections, arising from the presence of disorder; see Fig. 2(f). From these observations, two conclusions emerge naturally. First, the rephasing physics arises from disorder effects within the four-wave mixing process, i.e., vertex corrections. Second, not all vertex corrections have a rephasing nature, implying that only a partial rephasing is possible. In conclusion, rephasing in collective excitations is possible, although only partially, and thus one can also expect a similar, but not identical, almond-like signature in the echo peak, compare Fig. 2(b) and (d). Furthermore, from a theoretical point of view, disorder induced vertex corrections must be taken into account to capture rephasing effects.

III. NONLINEAR RESPONSE IN THE KELDYSH FORMALISM

This section provides a general introduction to the computation of third-order nonlinear responses in the Keldysh formalism, alongside an intuitive understanding of the diagrammatics involved. We follow closely throughout [84–87] for the field theory discussion and [15] for the nonlinear response. The structure of this section is as follows: In subsection III A, we introduce the generic φ^4 model to study the nonlinear response of collective bosonic excitations and discuss how to express nonlinear response functions as correlators in the Keldysh formalism. In III B, inspired by the lowest order approximation in interaction strength to the nonlinear response, we argue for the general diagrammatic structure of $\chi^{(3)}$.

A. Model and General considerations

We begin by considering a non-interacting relativistic action for a real scalar bosonic field φ of the form

$$S_0[\varphi] = \int_{\mathcal{C}} dt \int d^d \mathbf{r} \frac{1}{2} \left[(\partial_t \varphi)^2 - v^2 (\nabla \varphi)^2 - m_0^2 \varphi^2 \right], \quad (4)$$

where \mathcal{C} denotes the Keldysh contour, v the velocity, and m the mass. For further reference, the density of states of the theory is given by

$$\mathcal{N}(\epsilon) = \Theta(\epsilon - m_0) \frac{\mathcal{S}^d}{(2\pi)^d} \frac{\epsilon}{v^2} (\epsilon^2 - m_0^2)^{\frac{d}{2}-1}. \quad (5)$$

To perform the integral along the Keldysh contour we introduce two bosonic fields φ^+ and φ^- which reside in the forward and backward parts of the time contour, respectively. The non-interacting retarded, advanced and Keldysh Green's functions are given in the Keldysh ro-

tated basis $\varphi^\pm = \varphi^{\text{cl}} \pm \varphi^{\text{q}}$ by

$$i\mathcal{D}_0^{\alpha\beta}(\mathbf{r} - \mathbf{r}', t - t') = \int \mathbf{D}[\varphi] \varphi^\alpha(\mathbf{r}, t) \varphi^\beta(\mathbf{r}', t) e^{iS_0[\varphi^{\text{cl}}, \varphi^{\text{q}}]}, \quad (6)$$

with $\alpha, \beta = \{\text{cl}, \text{q}\}$, which further presents causality structure typical of the Keldysh propagator:

$$\mathcal{D}_0^{\alpha\beta} = \begin{pmatrix} \mathcal{D}_0^K(\mathbf{r} - \mathbf{r}', t - t') & \mathcal{D}_0^R(\mathbf{r} - \mathbf{r}', t - t') \\ \mathcal{D}_0^A(\mathbf{r} - \mathbf{r}', t - t') & 0 \end{pmatrix}. \quad (7)$$

Note that \mathbf{D} includes $1/\text{Tr}\{\rho_0\}$, with ρ_0 the equilibrium density matrix, following the standard Keldysh path integral measure [85]. Equivalently, the Green's functions in frequency-momentum representation are given by

$$\begin{aligned} \mathcal{D}_0^{R/A}(k, \omega) &= \frac{1}{2} \frac{1}{(\omega \pm i\eta)^2 - \epsilon_{\mathbf{k}}^2}, \\ \mathcal{D}_0^K(k, \omega) &= F(\omega) [\mathcal{D}_0^R(k, \omega) - \mathcal{D}_0^A(k, \omega)] \\ &= -\frac{i\pi}{2\epsilon_{\mathbf{k}}} \coth\left(\frac{\omega}{2T}\right) [\delta(\omega - \epsilon_{\mathbf{k}}) - \delta(\omega + \epsilon_{\mathbf{k}})]. \end{aligned} \quad (8)$$

Here, $\epsilon_{\mathbf{k}} = \sqrt{m_0^2 + v^2 k^2}$ is the bare energy-momentum dispersion relation, $\eta = 0^+$ is the (anti-)causal regularization, $F(\omega) = \coth(\omega/2T)$ is the equilibrium distribution function, and T is the temperature of the system. We consider an interaction between the bosons given by a generic φ^4 term:

$$\begin{aligned} S_{\text{int}}[\varphi] &= - \int_{\mathcal{C}} dt \int d^d \mathbf{r} \frac{g}{4!} \varphi^4 \\ &= - \int_{-\infty}^{\infty} dt \int d^d \mathbf{r} \frac{g}{3} [\varphi^{\text{cl}}(\varphi^{\text{q}})^3 + (\varphi^{\text{cl}})^3 \varphi^{\text{q}}]. \end{aligned} \quad (9)$$

In order to evaluate the response of the system to an external perturbation, we further introduce a drive/source term in the action given by

$$\begin{aligned} S_{\text{drive}}[\varphi, j] &= \int_{\mathcal{C}} dt \int d^d \mathbf{r} j \varphi \\ &= \int_{-\infty}^{\infty} dt \int d^d \mathbf{r} 2 (j^{\text{cl}} \varphi^{\text{q}} + j^{\text{q}} \varphi^{\text{cl}}), \end{aligned} \quad (10)$$

and define the partition function $Z[j]$ as

$$Z[j] = \int \mathbf{D}[\varphi^{\text{cl}}, \varphi^{\text{q}}] e^{iS[\varphi^{\text{cl}}, \varphi^{\text{q}}, j^{\text{cl}}, j^{\text{q}}] + iS_{\text{drive}}[\varphi, j]}, \quad (11)$$

where $S[\varphi, j] = S_0[\varphi] + S_{\text{int}}[\varphi]$. In the Keldysh formalism, the measured physical field is given by $\langle \varphi^{\text{cl}}(t) \rangle$ and the response functions are obtained by differentiation with respect to the physical sources j^{cl} . The third-order response function in the time-momentum space can be similarly computed by further differentiating with respect to classical sources:

$$\begin{aligned}\chi_{\mathbf{k};\mathbf{k}_1,\mathbf{k}_2,\mathbf{k}_3}^{(3)}(t_3,t_2,t_1) &= \frac{\delta^3 \langle \varphi_{\mathbf{k}}^{cl}(t_1+t_2+t_3) \rangle}{\delta j_{\mathbf{k}_3}^{cl}(t_1+t_2) \delta j_{\mathbf{k}_2}^{cl}(t_1) \delta j_{\mathbf{k}_1}^{cl}(0)} = -\frac{i}{2} \frac{\delta^4 Z}{\delta j_{\mathbf{k}}^q(t_1+t_2+t_3) \delta j_{\mathbf{k}_3}^{cl}(t_1+t_2) \delta j_{\mathbf{k}_2}^{cl}(t_1) \delta j_{\mathbf{k}_1}^{cl}(0)} \Big|_{j=0} \\ &= -8i \langle \varphi_{\mathbf{k}}^{cl}(t_1+t_2+t_3) \varphi_{\mathbf{k}_3}^q(t_1+t_2) \varphi_{\mathbf{k}_2}^q(t_1) \varphi_{\mathbf{k}_1}^q(0) \rangle,\end{aligned}\quad (12)$$

such that the expectation value of the boson field at time t is given by

$$\langle \varphi_{\mathbf{k}}^{cl}(t) \rangle^{(3)} = \frac{1}{L^{3d}} \sum_{\mathbf{k}_1,\mathbf{k}_2,\mathbf{k}_3} \int \frac{d\omega_1}{2\pi} \int \frac{d\omega_2}{2\pi} \int \frac{d\omega_3}{2\pi} \tilde{\chi}_{\mathbf{k};\mathbf{k}_1,\mathbf{k}_2,\mathbf{k}_3}^{(3)}(\omega_3,\omega_2,\omega_1) j_{\mathbf{k}_3}(\omega_3) j_{\mathbf{k}_2}(\omega_2) j_{\mathbf{k}_1}(\omega_1) e^{-i\bar{\omega}t}, \quad (13)$$

where we introduced the shorthand notation $\tilde{\chi}_{\mathbf{k};\mathbf{k}_1,\mathbf{k}_2,\mathbf{k}_3}^{(3)}(\omega_3,\omega_2,\omega_1) \equiv \chi_{\mathbf{k};\mathbf{k}_1,\mathbf{k}_2,\mathbf{k}_3}^{(3)}(\omega_1 + \omega_2 + \omega_3, \omega_2 + \omega_1, \omega_1)$. Note that causality imposes that $\chi^{(n)}(t_n, t_{n-1}, \dots, t_1) = 0$ if $t_j < 0$. Furthermore, in the absence of interactions, it is clear that Eq. (12) vanishes due to the presence of $\langle \varphi^q \varphi^q \rangle$ in all possible Wick contractions. We note that some of the results presented here can also be found in the context of the one-dimensional transverse field Ising model in [88].

B. Diagrammatic representation of $\chi^{(3)}$

In this work, we focus on the situation where the field perturbing the system, j , couples to the zero-momentum component of the bosonic field, φ , and measurements of the bosonic mode are also performed at $k = 0$. This is indeed the standard scenario when light is used to drive an excitation in a condensed matter system, for example in Ref. [58]. Therefore, we drop the spatial/momentum index in the rest of this subsection, understanding that light always couples to the collective excitation at zero momentum.

To lowest order in the interaction the third-order nonlinear response is given by (see Appendix A for a detailed derivation):

$$\tilde{\chi}_{\text{mf}}^{(3)}(\omega_1, \omega_2, \omega_3) = -g \chi^{(1)}(\omega_1) \chi^{(1)}(\omega_2) \chi^{(1)}(\omega_3) \chi^{(1)}(\bar{\omega}), \quad (14)$$

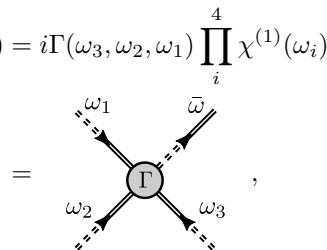
which readily recovers the ‘‘mean field’’ response obtained in [89] from an equations of motion formulation. Henceforth, we will use $\tilde{\chi}^{(3)}$ to denote the frequency shifted third-order response function, c.f. Eq (14). The diagrammatic representation of $\chi^{(3)}$ in Eq. (14) allows for a rather intuitive interpretation of the processes involved in the nonlinear response. The first-order perturbative calculation can be represented as

$$\tilde{\chi}_{\text{mf}}^{(3)}(\omega_3, \omega_2, \omega_1) = \begin{array}{c} \omega_1 \\ \swarrow \\ \cdot \\ \searrow \\ \omega_2 \end{array} \begin{array}{c} \bar{\omega} \\ \swarrow \\ \cdot \\ \searrow \\ \omega_3 \end{array} . \quad (15)$$

The dashed-to-solid line represents the retarded Green’s function of the boson and thus establishes the arrow of time. The dot simply denotes the nonlinearity strength g coming from the φ^4 term in the action. Thanks to the

built-in causality, the diagram Eq. (15) can naturally be interpreted as a four-wave mixing process. First, three collective modes with frequencies ω_1 , ω_2 , and ω_3 are excited in the material (note the possibility of oscillating at negative frequencies). At some point, the three excited modes are combined via a four-wave mixing process into a new mode with frequency $\bar{\omega} = \omega_1 + \omega_2 + \omega_3$ which then, propagates through the material; this is the mode that is eventually measured by the protocol. The separation between the incoming and outgoing modes is naturally built in the Keldysh formalism and provides an intuitive understanding of the processes involved in the nonlinear response.

From the diagrammatic representation of $\chi^{(3)}$ in Eq. (14) we expect that the full nonlinear susceptibility can be obtained by dressing the external propagators via the self-energy Σ and by including vertex corrections to the four-wave mixing process Γ , see Appendix B for a formal proof. That is, the external leg structure of the diagram remains the same; this can be depicted diagrammatically as

$$\tilde{\chi}^{(3)}(\omega_3, \omega_2, \omega_1) = i\Gamma(\omega_3, \omega_2, \omega_1) \prod_i^4 \chi^{(1)}(\omega_i)$$


$$= \begin{array}{c} \omega_1 \\ \swarrow \\ \Gamma \\ \searrow \\ \omega_2 \end{array} \begin{array}{c} \bar{\omega} \\ \swarrow \\ \Gamma \\ \searrow \\ \omega_3 \end{array}, \quad (16)$$

with the dressed propagator given by Dyson’s equation:

$$\text{---}\text{---}\text{---} = \text{---}\text{---}\text{---} + \text{---}\text{---}\text{---} \circ \Sigma \text{---}\text{---}\text{---}. \quad (17)$$

We thus conclude that once Γ and $\chi^{(1)}$ are known, we have fully determined the third-order nonlinear response. Furthermore, from this interpretation of the $\chi^{(3)}$ response, it becomes clear that the location of the peaks in the 2D map is determined by the excitation linewidth, or equivalently by the support of the imaginary part of the self-energy. The vertex Γ can only ‘‘redistribute’’ the weight in the vicinity of said support.

In this work, we adopt a conserving nonperturbative approach based on the Baym-Kadanoff construction [90, 91]. This allows us to obtain the vertex Γ and linear response $\chi^{(1)}$ in a self-consistent manner. However,

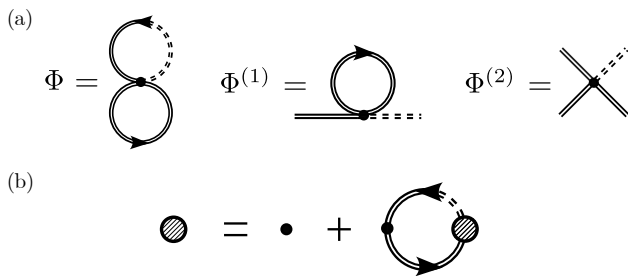


FIG. 3. (a) Luttinger-Ward functional approximation to lowest order in interaction and subsequent contributions to the self-energy and vertex. (b) Diagrammatic representation of the Bethe-Salpeter equation for the full vertex within the RPA approximation.

we envision that other nonperturbative approaches [92–94], such as the functional renormalization group, could be employed to obtain the 2D map beyond our current analysis.

To demonstrate the capabilities of our framework, we provide in the next section a derivation of $\chi^{(3)}$ in the absence of disorder, which already shows the effects of many-body correlations in the 2D map. The reader interested only in the effects of disorder in the nonlinear response, can directly proceed to Sec. V.

IV. RANDOM PHASE APPROXIMATION

As an initial demonstration of the computational capabilities of the formalism developed in the previous section we consider, in the absence of static disorder, the lowest-order conserving approximation in g , corresponding to the Random Phase Approximation (RPA). This section is divided into two subsections. The first subsection focuses on the detailed calculation of $\chi^{(3)}$ within the RPA, providing all the relevant diagrams and deriving the corresponding self-energy and vertex corrections. The second subsection examines the signatures of the 2D map peaks through both analytical results and numerical simulations, while elucidating important connections with linear response measurements and previous theoretical work [89].

A. $\chi^{(3)}$ within RPA

In this subsection, we employ the Keldysh formalism to compute $\chi^{(3)}$ within the (RPA). In order to have a conserving perturbative expansion, we begin by writing the lowest order approximation of the Luttinger-Ward functional and its resulting contributions to the self-energy and vertex, see Fig. 3.

1. Self-energy

The self-energy calculation results in a constant term (potentially diverging depending on the dimensionality)

$$\Sigma_g(\omega) = \frac{\delta\Phi[\mathcal{D}]}{\delta\mathcal{D}^R(\omega)} = \text{diagram} = \frac{ig}{L^d} \sum_{\mathbf{k}} \int \frac{d\Omega}{2\pi} \mathcal{D}_{\mathbf{k}}^K(\Omega) \quad (18)$$

which renormalizes the mass. We subsequently fix the renormalized bare mass m_0 to match the physically observed mass m .

2. Vertex

The bare vertex is obtained by cutting open two Green's function from the Luttinger-Ward functional, see (a) in Fig. 3, and it is simply given by

$$\Gamma^{(0)} = \frac{\delta^2\Phi[\mathcal{D}]}{\delta\mathcal{D}^K(\omega)\delta\mathcal{D}^R(\omega)} = \text{diagram} = ig, \quad (19)$$

compare with Eq. (A2).

3. Bubble

The bare bubble can be computed directly as

$$gB_0(\omega) = \text{diagram} = \frac{2ig}{L^d} \sum_{\mathbf{k}} \int \frac{d\Omega}{2\pi} \mathcal{D}_{\mathbf{k}}^R(\omega + \Omega) \mathcal{D}_{\mathbf{k}}^K(\Omega) \\ \simeq \frac{g}{2L^d} \sum_{\mathbf{k}} \frac{\coth(\frac{\epsilon_{\mathbf{k}}}{2T})}{\epsilon_{\mathbf{k}}} [\mathcal{D}_{\mathbf{k}}^R(\omega + \epsilon_{\mathbf{k}}) + \mathcal{D}_{\mathbf{k}}^R(\omega - \epsilon_{\mathbf{k}})],$$

where the second line is a good approximation when the imaginary part of the self energy is small, in this case when η is small since Σ is purely real. Motivated by the experiments on the Josephson plasmon of $\text{La}_{2-x}\text{Sr}_x\text{CuO}_4$ [58], we evaluate the relevant diagrams at $d = 2$, given that the density of states of the low energy Josephson plasmon model [95] presents the same structure as that of the φ^4 theory at $d = 2$, Eq. (5). Hence, in two dimensions and zero temperature, the bubble is given by

$$gB_0(\omega) = \frac{g}{2L^2} \sum_{\mathbf{k}} \frac{\coth(\frac{\epsilon_{\mathbf{k}}}{2T})}{\epsilon_{\mathbf{k}} [(\omega + i\eta)^2 - 4\epsilon_{\mathbf{k}}^2]} \\ = -\frac{g}{8\pi v^2} \frac{\tanh^{-1}(\frac{\omega + i\eta}{2m})}{\omega + i\eta}. \quad (20)$$

4. Third-order response

Collecting all the previously computed ingredients, the vertex correction is simply given by (note that the external legs have been amputated)

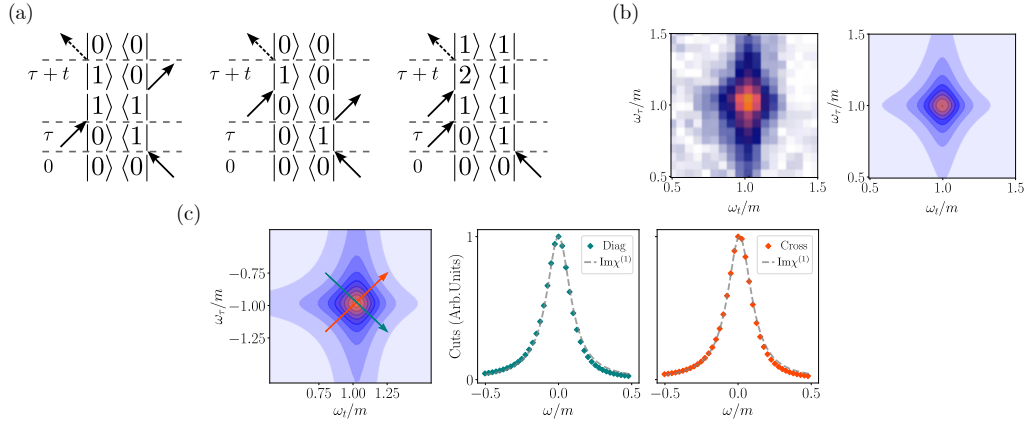


FIG. 4. (a) Two-sided Feynman diagrams for bosonic excitations. The solid arrows indicate the interaction with the first and second pulse E_A and E_B , while the dashed arrows represent the measurement. First two diagrams correspond to the ITLS-type paths, while the third is particular of bosonic excitations. Bosonic excitations can explore states beyond $|0\rangle$ and $|1\rangle$ resulting in asymmetric decay factors in τ and t , as discussed in Sec. IV B, and the possibility to end in a different state than the initial one after the protocol. (b) Nonrephasing peak experimentally obtained in Ref. [58] and theoretical nonrephasing peak from Eq. (23), with $\eta/m = 0.1$, displaying the vertical elongation typical of bosons. (c) Theoretically obtained absolute-value echo peak and its cuts along the diagonal (Diag) and cross diagonal (Cross). Both cuts follow the the spectral function of the single bosonic excitation $\text{Im}\chi^{(1)}$, in dashed gray, when the vertex corrections are small.

$$i\Gamma_{\text{RPA}}(\omega_3, \omega_2, \omega_1) = \frac{\bullet}{1 - \text{loop}(\omega_1 + \omega_2)} + \text{permutations} - 2 \bullet, \quad (21)$$

and we arrive directly at the third-order response

$$\chi_{\text{RPA}}^{(3)}(\omega_1 + \omega_2 + \omega_3, \omega_1 + \omega_2, \omega_1) = \underbrace{\left(2g - \sum_{i=1}^3 \frac{g}{1 - gB_0(\omega_1 + \omega_2 + \omega_3 - \omega_i)}\right)}_{i\Gamma_{\text{RPA}}(\omega_3, \omega_2, \omega_1)} \chi^{(1)}(\omega_1)\chi^{(1)}(\omega_2)\chi^{(1)}(\omega_3)\chi^{(1)}(\bar{\omega}), \quad (22)$$

with $\chi^{(1)}$ given by Dyson's equation, see Eq. (17). Note that for $B_0 \ll 1$, the RPA result asymptotically approaches the lowest order or “mean field” calculation, see Eq. (14). In the classical limit, $T \gg \epsilon_{\mathbf{k}}$, this result is the analogue of the sum of both “mean field” and “squeezing” contributions presented in [89]. As such, it serves as a generalization to the quantum limit and shows that the Gaussian state Ansatz for $\chi^{(3)}$ corresponds to a ver-

tex correction within the RPA.

B. 2D maps within the RPA

The tree level approximation of the nonlinear response, see Eq. (14), provides a reasonable approximation of the 2D map when the nonlinearity g is small. Assuming a finite broadening η , the map is given by

$$S(\omega_t, \omega_\tau) \sim \frac{2(6\eta - i(\omega_t + 3\omega_\tau))}{(-i\eta + m - \omega_t)(-3i\eta + m - \omega_t)(i\eta + m + \omega_t)(3i\eta - 3m + \omega_t)(3i\eta + m + \omega_t)(3i\eta + 3m + \omega_t)(-i\eta + m - \omega_\tau)(i\eta + m + \omega_\tau)}. \quad (23)$$

This expression provides valuable insights into key aspects of the 2D map for nonlinear collective excitations. First, the poles in Eq. (23) exhibit a damping given by

η or 3η , instead of the expected η from the ITLS perspective. The appearance of these two different damping rates can be understood by tracing the different path-

ways contributing, for instance, to the echo response, see Fig. 4(a) for a two-sided Feynman diagram interpretation. We identify the terms proportional to $e^{-\eta(\tau+t)}$ as the prototypical echo peaks of ITLS, corresponding to the first two paths in Fig. 4(a). However, we also obtain an additional contribution proportional to $e^{-\eta(\tau+3t)}$, which corresponds to the last path in Fig. 4(a). Note that this term contains a larger decay rate during the second time delay due to the fact that three excitations are coexisting during this time evolution. Since this extra path comes with a relative minus sign with respect to the previous two, adding up the three contributions results in an elongated peak along the τ axis (vertically), as can be seen in Fig. 4 (b), where we present the experimentally observed nonrephasing peak in [58] and the analytically obtained following Eq. (23). Such contribution is absent in the ITLS scenario, and the peaks are fully symmetric. One may also wonder why they come with the same numerical factors into Eq. (23) even though there are two diagrams that contribute to the ITLS-type and one to the other. This is due to the Bose enhancement factors arising in the absorption and emission to and from the $|2\rangle$ state. This results in an extra factor of 2 that balances the contributions. Note that this vertical elongation effect is not limited to the tree-level calculation, but it generally appears in the 2D maps of bosonic excitations [89].

Even more remarkable and of practical interest is the fact that if vertex corrections are moderate, the cuts along the diagonal and cross-diagonal of the echo peak coincide with each other and with the excitation linewidth, i.e., with the linear response broadening. To illustrate this point, we plot in Fig. 4(c) the absolute-value echo peak and its cuts as well as the imaginary part of the linear response function for the full RPA response, Eq. (22), with moderate nonlinearity $g/m^2 = 0.1$. As can be seen, the overlap is remarkably accurate; note the absence of any fitting parameters in the comparison. We expect this feature to break down as soon as vertex corrections start to play an important role, since the nonlinear response directly depends on the vertex function; see Eq. (B10). One of the main contributions of the vertex is the inclusion of scattering corrections, as we will see in the upcoming sections. Therefore, the 2D map contains relevant information about the scattering processes between the nonlinear collective modes and it can reveal intriguing phenomena, such as bound state formation, the discussion of which will be presented elsewhere.

V. ELASTIC SCATTERING

This section provides a quantitative discussion of the effects of static disorder in the 2D maps of collective excitations. The first subsection VA, is devoted to building an intuitive understanding of the necessary subclass of diagrams essential to capture the rephasing physics. In the second subsection VB, we obtain the self-energy and full disorder vertex in the sole presence of disorder. Then,

in the third subsection VC, we extend the diagrammatic calculation of $\chi^{(3)}$ to account for the disorder-induced corrections to the self-energy and vertex. The fourth subsection VD focuses on the signatures of the echo peak for correlated collective excitations, with particular emphasis on comparing and highlighting the striking differences between these signatures and those of more familiar uncorrelated excitations typical of ITLS.

We consider an elastic scattering term in the action given by

$$\begin{aligned} S_{\text{dis}} &= - \int_{\mathcal{C}} dt \int d^d \mathbf{r} \frac{V(\mathbf{r})}{2} \varphi^2(\mathbf{r}, t) \\ &= - \int_{-\infty}^{\infty} dt \int d^d \mathbf{r} 2V(\mathbf{r}) \varphi^{\text{cl}}(\mathbf{r}, t) \varphi^q(\mathbf{r}, t), \end{aligned} \quad (24)$$

and assume a disorder distribution which is Gaussian and flat, i.e., $\overline{V} = 0$ and $\overline{V(\mathbf{r})V(\mathbf{r}')} = V_0^2 \delta(\mathbf{r} - \mathbf{r}')$. Here, $V_0^2 = V^2 \xi^d$, where V^2 characterizes the strength of the disorder and ξ its (short-range) correlation length. Integrating out the disorder results in a φ -dependent action, with an effective disorder induced vertex given by

$$\begin{aligned} S_{\text{dis}}^{\text{eff}}[\varphi] &= i \int dt \int dt' \int d\mathbf{r} 2V_0^2 \\ &\quad \times \varphi^{\text{cl}}(\mathbf{r}, t) \varphi^q(\mathbf{r}, t) \varphi^{\text{cl}}(\mathbf{r}, t') \varphi^q(\mathbf{r}, t'). \end{aligned} \quad (25)$$

The disorder vertex does not directly contribute to the non-linear response $\chi^{(3)}$ by its own due to its causality structure. Specifically, this implies that there is no leading term in $\chi^{(3)}$ solely proportional to V_0^2 .

A. Diagrammatic intuition of the echo peak

We expand here the intuitive discussion of Sec. II by adapting it to the language of diagrammatics, and justify the subclass of diagrams necessary to capture the echo signature. As previously argued, the origin of the almond-like structure of the echo peak relies on the system evolving with opposite frequencies during time delays τ and t . Following the notation set by Eq. (2), the first (second) time delay τ (t) is dominated by the dynamics of ω_1 ($\bar{\omega}$). This can intuitively be understood since during the first time delay, only the first pulse (ω_1) has interacted with the system, while for the second time delay, the effect of both pulses ($\bar{\omega}$) is present. Combining this with the diagrammatic representation in Eq. (16), we deduce that the diagrams that have a rephasing nature are the ones correlating propagators with frequency ω_1 and $\bar{\omega}$, see Fig. 5(a). However, there are other diagrams which lack this rephasing structure, specifically those that correlate propagators other than the ones with frequencies ω_1 and $\bar{\omega}$, see Fig. 5(b) for two examples. Therefore, we do not expect perfect rephasing of the collective excitation, even in the sole presence of static disorder, in contrast to the ITLS scenario.

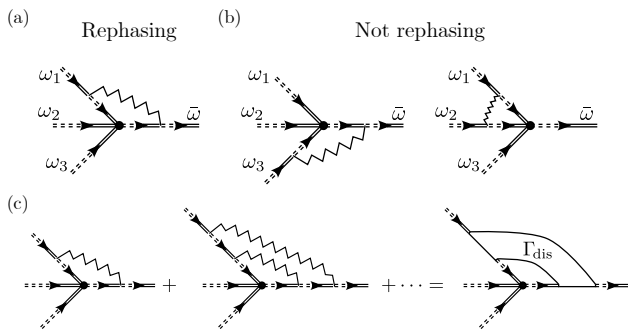


FIG. 5. Intuition behind the diagrams for the echo peak. In (a) a disorder line correlates ω_1 , which corresponds to the first time oscillation, with $\bar{\omega}$, which corresponds to the second time delay oscillation. This results in the diagram presenting the rephasing structure. In (b) two examples of vertex corrections that do not correlate ω_1 with $\bar{\omega}$, resulting in contributions that do not exhibit the rephasing structure. In (c) the nonperturbative ladder approximation for the disorder that we consider in this work.

As we discuss in Sec. V C, in order to capture the effects of disorder, it is not enough to consider the lowest order disorder corrections. This is due to the intrinsically nonperturbative character of disorder effects [96]. In this work, we consider the ladder resummation of the previously discussed class of diagrams, i.e., the infinite series of noncrossing disorder lines, see Fig. 5(c). By considering the infinite set of disorder lines connecting the first and last excitation, we enhance the correlations between them which results in a dramatic increase of the rephasing. In the next subsection, we proceed to perform the ladder resummation of the disorder effects without considering nonlinearity.

A second family of diagrams involving impurity scattering crossings can be considered beyond the ladder approximation. However, similar arguments to the fermionic counterpart can be applied to safely disregard them in the limit of $E\tau_e \gg 1$ [96, 97], where E is the typical excitation energy and τ_e the elastic collision time, which can be associated to the decay time of the single-boson propagator. The typical energy scale can be associated to the boson mass $E \sim m$, and the typical collision time $\tau_e^{-1} \sim V_0^2/v^2m$ can be obtained from the Born approximation to the impurity scattering, see Eq. (28). The validity of the ladder approximation thus relies on $(mv/V_0)^2 \gg 1$.

B. Ladder resummation of disorder

The Luttinger-Ward functional for the noninteracting disordered system is depicted in Fig. 6. By performing a derivative of the functional with respect to $\mathcal{D}^R(\omega)$ we obtain the self-consistent self-energy within the Born

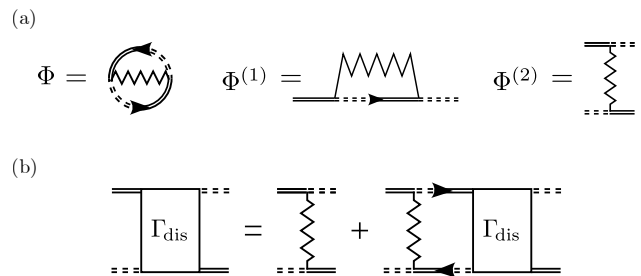


FIG. 6. (a) Luttinger-Ward functional approximation to lowest order in disorder. (b) Bethe-Salpeter equation for the disorder vertex.

(noncrossing) approximation ($v = 1$ henceforth),

$$\begin{aligned} \Sigma_V^R(\omega) &= \text{diagram} = \frac{4V_0^2}{L^d} \sum_{\mathbf{k}} \mathcal{D}_{\mathbf{k}}^R(\omega) \\ &= \frac{V_0^2}{2\pi} (\log(\Lambda) - \log(\omega^2 - m^2 - \Sigma_V^R(\omega))), \end{aligned} \quad (26)$$

where we introduce an UV momentum cutoff and consider it the largest scale in the problem. The self-consistent solution gives a real contribution to the self-energy which effectively renormalizes the mass term. To find the renormalized (physical) mass we utilize on-shell renormalization and introduce a counterterm δ_m that relates the physical mass m to the bare one m_0 by $m^2 = m_0^2 + \text{Re} \Sigma_V(m) - \delta_m$, leading to

$$\delta_m = m_0^2 - m^2 + \text{Re} \{ \Sigma_V^R(m) \}. \quad (27)$$

The counterterm allows us to safely take the limit $\Lambda \rightarrow \infty$, resulting in the self-energy:

$$\Sigma_V^R(\omega) = -i \frac{V_0^2}{2} \text{sgn}(\omega). \quad (28)$$

This demonstrates that the net effect of disorder is to introduce a finite lifetime to the excitation $-2 \text{Im} \Sigma_V^R(m) = V_0^2$.

Having obtained the disorder contribution to the self-energy, we proceed to compute vertex correction in the $cl-q-cl-q$ channel. The bare disorder vertex $\Gamma_{\text{dis}}^{(0)}$ can be obtained within the Baym-Kadanoff formalism by taking a functional derivative of the self-energy,

$$\Gamma_{\text{dis}}^{(0)}(\mathbf{k}; \omega_a, \omega_b) = \frac{\delta \Sigma_V^R(\omega_a)}{\delta \mathcal{D}_{\mathbf{k}}^R(\omega_b)} = \text{diagram}. \quad (29)$$

Finally, to obtain the full disorder vertex Γ_{dis} we solve the Bethe-Salpeter equation which is depicted in Fig. 6(b),

$$\Gamma_{\text{dis}}(\mathbf{k}; \omega_a, \omega_b) = \frac{2V_0^2}{1 - V_0^2 \lambda_0(\mathbf{k}; \omega_a, \omega_b)}, \quad (30)$$

where we have introduced the disorder bubble:

$$\lambda_0(\mathbf{k}; \omega_a, \omega_b) = \frac{4}{L^d} \sum_{\mathbf{q}} \mathcal{D}_{\mathbf{k}+\mathbf{q}}^R(\omega_a) \mathcal{D}_{\mathbf{q}}^R(\omega_b). \quad (31)$$

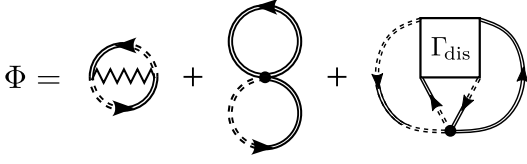


FIG. 7. Luttinger-Ward functional employed for the computation of $\chi^{(3)}$ in the presence of elastic scattering. In addition to the RPA contribution and the disorder contribution, the last term corresponds to an interaction-disorder term.

In two dimensions the disorder bubble can be computed at vanishing momentum for an arbitrary momentum independent self-energy

$$\lambda_0(\mathbf{0}; \omega_a, \omega_b) = \frac{1}{4\pi} \frac{\log \left[m^2 + \frac{\Sigma_V^R(\omega_a)}{2} - \omega_a^2 \right] - \log \left[m^2 + \frac{\Sigma_V^R(\omega_b)}{2} - \omega_b^2 \right]}{\frac{\Sigma_V^R(\omega_a)}{2} - \frac{\Sigma_V^R(\omega_b)}{2} - \omega_a^2 + \omega_b^2}. \quad (32)$$

Having obtained the RPA resummation without disorder and the full disorder vertex without interaction, we proceed to compute the effects of disorder on the nonlinearity.

C. $\chi^{(3)}$ with elastic scattering

To capture the echo physics it is essential to include disorder corrections to the interaction vertex, as discussed in Sec. II. This is achieved by introducing an additional disorder-interaction contribution to the Luttinger-Ward functional illustrated in Fig. 7. Specifically, we incorporate the infinite series of noncrossing disorder diagrams into the functional by using Γ_{dis} instead of $\Gamma_{\text{dis}}^{(0)}$. Notably, the $\chi^{(3)}$ obtained when considering only $\Gamma_{\text{dis}}^{(0)}$ does not exhibit the almond-like signature in the echo peak, although it provides an instructive hint toward the correct physical mechanism. For completeness, the details of this calculation, along with the resulting 2D map signatures, are presented in Appendix C. The necessity to consider Γ_{dis} underscores the non-perturbative nature of the echo peak signature in relation to disorder and highlights the potential of 2D spectroscopy as a tool for probing more complex disorder effects. We will explore this in greater detail in a forthcoming publication. Following the same structure as in Sec. IV we proceed to evaluate the necessary diagrams to obtain $\chi^{(3)}$ in the presence of disorder.

1. Self-energy

The interaction and disorder-only contributions to the self-energy arising from the Luttinger-Ward functional are given by Eqs. (18) and (26) respectively. There are two additional contributions coming from the disorder-interaction part:

$$\begin{aligned} \Sigma_{g-V}^R(\omega) &= \text{Diagram 1} + \text{Diagram 2} \\ &= 2 \times \frac{4ig}{L^{2d}} \sum_{\mathbf{k}, \mathbf{q}} \int \frac{d\Omega}{2\pi} \Gamma_{\text{dis}}(\mathbf{q}; \omega, \Omega) \mathcal{D}_{\mathbf{k}}^R(\omega) \mathcal{D}_{\mathbf{q}-\mathbf{k}}^R(\Omega) \mathcal{D}_{\mathbf{q}}^K(\Omega). \end{aligned} \quad (33)$$

In order to determine the full Green's function we numerically solve the self-consistent Dyson equation with $\Sigma_{\text{tot}}^R = \Sigma_g^R + \Sigma_V^R + \Sigma_{g-V}^R$.

2. Vertices

The bare vertices contributing to the nonlinear response are given by taking a derivative with respect to the Keldysh Green's function. The RPA contribution is given in Eq. (19) and the interaction-disorder contribution to the Luttinger-Ward results in the following vertices:

$$\begin{aligned} \text{Diagram 1} &= ig \left(\frac{4}{L^d} \sum_{\mathbf{k}} \mathcal{D}_{\mathbf{k}}^R(\omega_a) \mathcal{D}_{-\mathbf{k}}^R(\omega_b) \right) \Gamma_{\text{dis}}(\mathbf{0}; \omega_a, \omega_b) \\ &= ig \frac{2V_0^2 \lambda(\mathbf{0}; \omega_a, \omega_b)}{1 - V_0^2 \lambda(\mathbf{0}; \omega_a, \omega_b)} \\ \text{Diagram 2} &= ig \left(\frac{4}{L^d} \sum_{\mathbf{k}} \mathcal{D}_{\mathbf{k}}^R(\omega_a) \mathcal{D}_{\mathbf{k}}^R(\omega_b) \right) \Gamma_{\text{dis}}(\mathbf{0}; \omega_a, \omega_b) \\ &= ig \frac{2V_0^2 \lambda(\mathbf{0}; \omega_a, \omega_b)}{1 - V_0^2 \lambda(\mathbf{0}; \omega_a, \omega_b)}. \end{aligned} \quad (34)$$

Note that we have employed the inversion symmetry of our system, $\epsilon_{\mathbf{k}} = \epsilon_{-\mathbf{k}}$. Here, $\lambda(\mathbf{0}; \omega_a, \omega_b)$ indicates that we use the full self-energy in Eq. (32) as opposed to $\lambda_0(\mathbf{0}; \omega_a, \omega_b)$.

3. Bubbles

The bare bubble arising from the RPA contribution is given by Eq. (20). The additional interaction-disorder term gives rise to a second bubble given by:

$$\begin{aligned}
gB_{\text{dis}}(\omega) &= \text{Diagram} = 2ig \int \frac{d\Omega}{2\pi} \left(\frac{1}{L^d} \sum_{\mathbf{q}} \mathcal{D}_{\mathbf{q}}^R(\omega + \Omega) \mathcal{D}_{\mathbf{q}}^K(\Omega) \right) \left(\frac{4}{L^d} \sum_{\mathbf{q}} \mathcal{D}_{\mathbf{q}}^R(\omega + \Omega) \mathcal{D}_{\mathbf{q}}^R(\Omega) \right) \Gamma_{\text{dis}}(\mathbf{0}; \omega + \Omega, \omega) \\
&= 2ig \int \frac{d\Omega}{2\pi} \left(\frac{1}{L^d} \sum_{\mathbf{q}} \mathcal{D}_{\mathbf{q}}^R(\omega + \Omega) \mathcal{D}_{\mathbf{q}}^K(\Omega) \right) \frac{2V_0^2 \lambda(\mathbf{0}; \omega + \Omega, \Omega)}{1 - V_0^2 \lambda_0(\mathbf{0}; \omega + \Omega, \Omega)}. \tag{35}
\end{aligned}$$

This concludes the calculation of all the necessary ingredients to compute $\chi^{(3)}$ in the presence of disorder within our conserving approximation.

4. Third-order response

Collecting all the pieces together, the vertex $i\Gamma$ is diagrammatically given by

$$\begin{aligned}
i\Gamma(\omega_3, \omega_2, \omega_1) &= \text{Diagram 1} + \text{Diagram 2} + \text{permutations} - 2 \cdot \text{Diagram 3} - \text{Diagram 4}, \tag{36} \\
&= \text{Diagram 1}(\omega_1, \omega_2) + \text{Diagram 2}(\omega_3, \bar{\omega}) \\
&\quad - \text{Diagram 3}(\omega_1 + \omega_2) - \text{Diagram 4}(\omega_1 + \omega_2)
\end{aligned}$$

where permutations refer to unique pairs without accounting for the frequency ordering. In total there exist three of such permutations.

D. 2D maps with elastic scattering

Having obtained the vertex and self-energy in the presence of static disorder, we proceed to compute the nonrephasing and rephasing (echo) peaks by means of Eq. (2). In Fig. 8(a) and (b) we present the evolution of the nonrephasing and echo peaks respectively as a function of disorder strength for a fixed nonlinearity $g/m^2 = 0.01$. While the nonrephasing peak only becomes broader following the excitation linewidth, the echo peak exhibits the characteristic almond shape, qualitatively analogous to the ITLS signature. In the latter case of ITLS, the presence of inhomogeneous broadening results in a symmetric broadening of the nonrephasing peak, while the echo peak reveals the presence of disorder through its distinctive asymmetric almond-like shape. However, a key difference of these spectra from the ITLS scenario is that the shape of the echo peak in the many-body case remains roughly unchanged as disorder increases. The only effect of increasing disorder is an overall scaling of the peak, c.f. 8(b). We present in the left panel of Fig. 8(c) the evolution with disorder of the ratio between the full width at half maxima (FWHM) of the diagonal and cross-diagonal cuts of echo peak (α) for $g/m^2 = 0.01$ in the collective excitation scenario (CE). The ratio α stays roughly constant as disorder grows, highlighting that the almond-like signature does not become more asymmetric between the diagonal and cross-diagonal. This differs significantly from the case of ITLS, also shown in the left panel of Fig. 8(c),

where one expects this ratio to decrease for increasing disorder. For the localized excitation scenario we choose for comparison purposes $\sigma^2 = V_0^2$ and a finite value for the homogeneous broadening $\gamma/m = 0.1$ such that the ratios for both situations are comparable given the same initial value of $V_0^2/m^2v^2 = 0.2$.

To gain a deeper understanding regarding this intriguing scaling invariance feature, we plot in the middle panel of Fig. 8(c) the FWHM of the diagonal and cross-diagonal cuts as a function of V_0^2 for $g/m^2 = 0.01$. As the elastic scattering strength is increased, the resulting difference between the widths of the cross-diagonal and diagonal also increases such that their ratio α is kept constant. Lastly, we plot in the right panel of Fig. 8(c), the evolution of the ratio α for different values of V_0^2 as a function of nonlinearity strength g . This plot reveals a rather striking feature: The asymmetry between the diagonal and cross diagonal FWHM is rather insensitive to the strength of g and V_0^2 , at least within our approximation, and results in a robust value of the ratio $\alpha \approx 0.75$.

A further subtle but important difference with respect to the ITLS scenario lies in the asymmetry of the almond-like signature across the diagonal. In the ITLS case, the Larmor frequencies are typically assumed to follow a Gaussian distribution, leading to a symmetric echo peak with respect to reflections along the cross-diagonal, c.f. Fig. 2. In contrast, for collective excitations driven at zero momentum, there are no finite momentum states below the mass available to be scattered into via the static disorder. Consequently, the explored virtual states al-

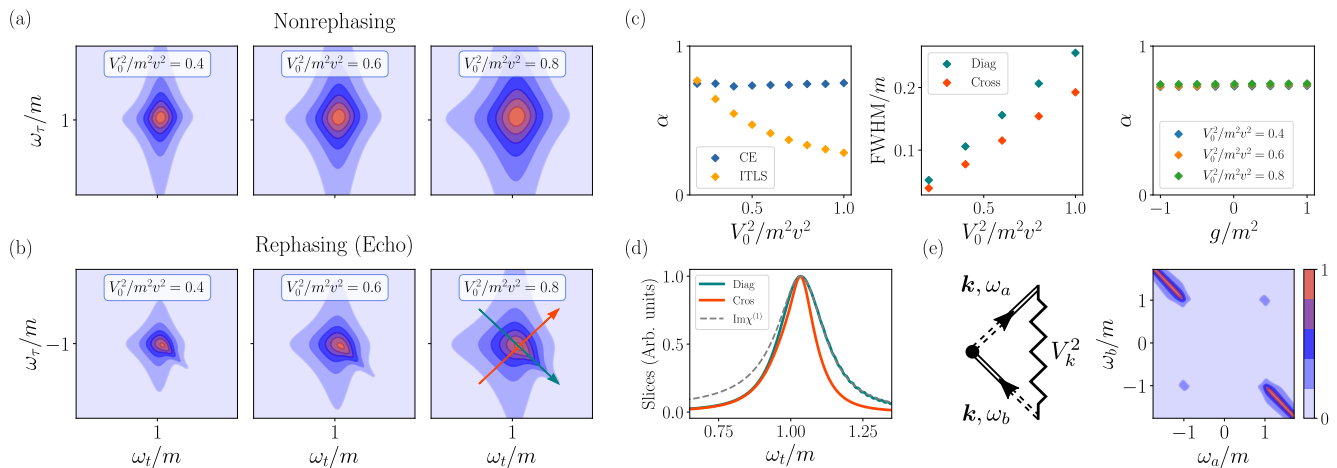


FIG. 8. (a)-(b) Evolution of the Nonrephasing and Rephasing (Echo) peaks as the disorder strength V_0^2 increases for $g/m^2 = 0.01$. The Nonrephasing peak (a) becomes broad in the presence of disorder while the Echo peak (b) displays the characteristic almond-like signature signaling the origin of the broadening to be elastic scattering. (c) Left panel: comparison between the ratio of the FWHM along the diagonal and cross-diagonal for the collective excitation (CE) and ITLS scenarios. While the ratio decreases for the ITLS case, in the Many-body scenario the ratio stays roughly constant. Central panel: Extracted FWHM for the diagonal and cross-diagonal slices of the echo peak as a function of elastic scattering strength for $g/m^2 = 0.01$. The FWHM increase in such a way that their ratio remains fixed. Right Panel: α as a function of nonlinearity g for different values of V_0^2 . The ratio $\alpha \approx 0.75$ is roughly independent of the values of g and V_0^2 , a robust feature in our perturbative regime of small g . (d) Slices along the diagonal (teal) and cross-diagonal (orange) of the echo peak for $g/m^2 = 0.01$ and $V_0^2/m^2v^2 = 0.8$. The dashed gray line represents the the spectral function $\text{Im}\chi^{(1)}$, which coincides with the cut along the diagonal for energies larger than the mass. (e) Diagram and color-plot of the absolute value of the tree-level vertex correction in the presence of disorder. The vertex correction is most prominent along the $\omega_a = -\omega_b$ line heralding the echo nature of the process.

ways have higher energies, resulting in an almond shape which is elongated exclusively towards higher energies, c.f. Fig. 8(b). This becomes especially evident when considering the slices of the echo peak across both diagonals, see Fig. 8(d). We note that this asymmetry is compatible with the echo peak experimentally measured in [58]. Furthermore, we also plot in Fig. 8(d) the linear response in dashed gray and note that it coincides with the diagonal cut at frequencies larger than the mass. This is in stark contrast to the discussion in IV B, where in the absence of strong vertex corrections both diagonal and cross diagonal cuts are equivalent and coincide with the spectral function.

In agreement with the intuition put forward in Sec. II, we find from a quantitative perspective that the central ingredient to capturing rephasing effects in the echo peak lies in the vertex corrections induced by the static disorder. In Fig. 8(e) we present a color plot of the absolute-value disorder-corrected vertex. As can be directly seen, the contribution is most notable in the vicinity of $\omega_a = -\omega_b$ and for $|\omega_a|, |\omega_b| > m$. This asymmetry between the two diagonals, favoring opposite sign frequencies, heralds the echo physics contained in the vertex correction and, in turn, is responsible for the appearance of the characteristic almond-shaped peak in the echo nonlinearity. Note however, that although the system is solely subjected to static disorder, or equivalently elastic scattering, we do not observe a perfect rephasing, i.e., an infinitely sharp peak along the diagonal. We thus con-

clude that, although a perfect echo signature is unattainable for collective excitations, the almond-shaped signature can still be employed to identify broadening caused by elastic scattering.

As a final remark, we highlight that using the standard fitting forms for ITLS [83] on the peaks in Fig. 8, and interpreting the extracted inhomogeneous broadening as the disorder of the system, would lead to incorrect conclusions. Even though the excitation only experiences disorder, its broadening effects on the linewidth are misinterpreted by the fitting procedure as a homogeneous contribution. One would thus conclude that the excitation suffers from both homogeneous and inhomogeneous broadening although only elastic scattering is present. Hence, it is clear that, in the case of collective excitations, using the concepts of homogeneous and inhomogeneous broadening is misleading. We advocate, in this case, for the use of the more appropriate concepts of elastic and inelastic scattering.

VI. DISENTANGLING ELASTIC AND INELASTIC SCATTERING

Having investigated the effects of elastic scattering in the previous section, we now examine the scenario where both elastic and inelastic scattering are present, focusing on the signatures of the echo peak. In principle, inelastic scattering processes can further contribute to the self-

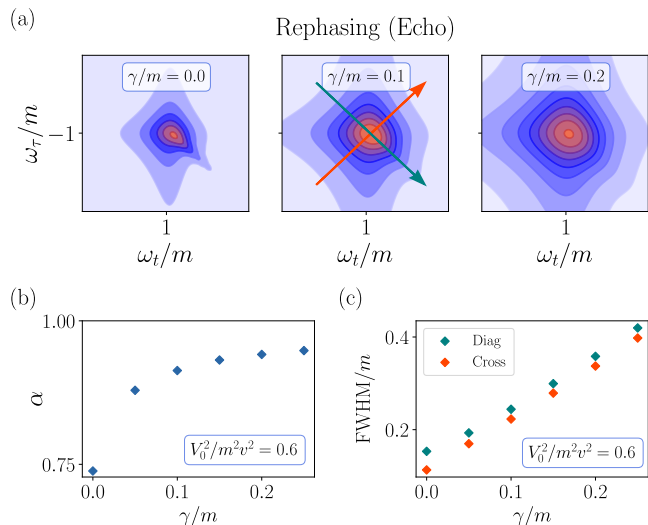


FIG. 9. (a) Evolution of the Rephasing (Echo) peak as the inelastic scattering strength γ increases. The Nonrephasing peak which displays a significant almond-like signature in the absence of inelastic scattering starts losing the asymmetry as disorder is increased. (b) Evolution of the ratio between the diagonal and cross-diagonal FWHM, α . As the inelastic scattering increases, the echo peak signature becomes more symmetric asymptotically tending towards $\alpha = 1$. (c) Evolution of the FWHM of both the diagonal and cross-diagonal cuts as a function of γ for fixed $g/m^2 = 0.01$ and $V_0^2/m^2v^2 = 0.6$. When γ is increased the two widths grow while keeping their difference approximately fixed.

energy and vertex of the collective mode. However, vertex corrections can be safely disregarded in two different scenarios: when the collective mode is coupled to another massive collective mode with a significantly larger mass, and when it is coupled to a continuum of quasiparticles with a density of states sharply peaked at energies higher than the mass. In Appendix D, we provide a microscopic model for the former and demonstrate the irrelevance of vertex corrections in this situation. Thus, we treat inelastic scattering processes as an incoherent bath, adding to the self-energy of the collective excitation a phenomenological damping term of the form $i\omega\gamma$.

Building on the limits of elastic and inelastic scattering discussed in Sec. V and IV, respectively, we analyze the echo peak signatures as a function of V_0^2 and γ , for a fixed nonlinear strength g . The behavior of the echo peak in the presence of both elastic and inelastic scattering can be inferred from the results of the limiting scenarios. The elastic scattering strength V_0^2 contributes asymmetrically to the echo peak, while the inelastic strength γ contributes symmetrically. The competition between these two effects determines the overall shape of the peak. In Fig. 9(a), we present the evolution of the echo peak as the inelastic scattering increases, with a finite fixed elastic scattering strength $V_0^2/m^2v^2 = 0.6$. The increase in inelastic scattering washes away the almond-like signature, and the peak becomes more symmetric, approach-

ing $\alpha \rightarrow 1$ in the inelastic-dominated limit, see Fig. 9(b). To gain intuition and disentangle the effects of the scatterings, we present in Fig. 9(c) the FWHM of both the diagonal and cross-diagonal cuts as a function of γ for a fixed V_0^2 . For a fixed elastic scattering strength, the FWHMs stay roughly parallel as γ increases, that is, their difference stays constant. Furthermore, the increase of the widths is linear with γ , at least within our approximation, as shown in Fig. 9. This signature indicates that the only processes activated – e.g. by increasing the temperature – are inelastic scattering events, under the reasonable assumption that the disorder strength remains constant.

In conclusion, for a fixed disorder, an increase in γ leads to a less pronounced almond-like signature, indicated by a larger α . This process can also be identified by investigating FWHMs that grow linearly with increasing γ . Furthermore, the robustness of α in both the elastic and inelastic scattering limits, as a function of g and V_0^2 , allows to quantify the presence and relative strength of each scattering processes.

VII. CONCLUSIONS AND OUTLOOK

In this paper, we have introduced a new framework for understanding disorder effects in the nonlinear response of collective many-body bosonic excitations. Specifically, we have shown that the standard framework used for interpreting two-dimensional spectroscopy, originally developed for isolated two-level systems, breaks down in the presence of many-body correlations. In particular, we have emphasized two main points: (i) the necessity to depart from the concepts of homogeneous and inhomogeneous broadening in favor of elastic and inelastic scattering, and (ii) the impossibility of achieving perfect rephasing in the echo nonlinearity, even in the sole presence of elastic scattering. We have then developed a quantitative field-theoretical approach to calculate the third order nonlinear response within the Keldysh formalism and used it to compute the spectra of two-dimensional terahertz spectroscopy of collective excitations. Through a perturbative treatment of static disorder, we have demonstrated that the echo peak exhibits an almond-like signature, while confirming that perfect rephasing cannot be attained. Finally, we have provided detailed experimental signatures in two-dimensional spectroscopy when both elastic and inelastic scattering processes are present. These signatures can readily be employed to investigate experimental echo nonlinearities, assisting in identifying and quantifying different sources of broadening for bosonic collective excitations in many-body systems.

Of particular interest, and serving both as the motivation and inspiration for this work, is the study of the effects of spatial inhomogeneity in the superfluid density on the Josephson plasmon excitations of high temperature superconducting cuprates. Specifically, the recent ex-

perimental realization of two-dimensional terahertz spectroscopy for the Josephson plasmon of $\text{La}_{2-x}\text{Sr}_x\text{CuO}_4$ near optimal doping has unearthed intriguing features of the echo peak as a function of temperature [58]. These results offer an ideal platform for applying our theoretical developments to extract valuable insights into the nature and effects of disorder in cuprates. This work is currently under development and will be presented in a forthcoming publication.

We envision that our work on two-dimensional spectroscopy of collective bosonic excitations can serve as a foundation for investigating several intriguing open questions. A natural extension of this work would be to explore the impact of real space localization of collective excitations on the echo peak. In this limit, the standard treatment used in isolated two-level systems could become accurate, allowing for a perfect rephasing and potentially serving as a probe of localization. Of particular interest could be the study of the nonlinear response of disordered Bose-Einstein condensates, where Anderson localization has been observed in the past [98, 99]. Nonlinear spectroscopy could provide a new framework for understanding the impact of nonlinearities on disordered systems, potentially leading to new insights into many-body localization [53]. Similarly to how multidimensional-coherent spectroscopy probes biexcitons and trions [30–32], two-dimensional terahertz spectroscopy could be envisioned as a tool to investigate bound states of bosonic collective excitations, for instance biphonons or biplasmons. Extending our approach to fifth-order nonlinearities would capture the rephasing of two-quantum coherences and open avenues for studying the effects of disorder on bound states. [100]. Furthermore, inspired by the capabilities of two-dimensional spectroscopy, a promising direction would be to study the coupling and hybridization between different fields. For instance, extending the current analysis to models with several coupled low-energy excitation could elucidate unique features of interacting

fields.

Recent advancements have shown that dynamic manipulation of quantum materials using light can induce non-trivial correlated phases [101], such as light-induced ferroelectricity [102, 103] or superconductivity [104–106] among many others. These out-of-equilibrium phenomena present new challenges for understanding the intricate dynamics that govern them. Our formulation within the Keldysh formalism provides an ideal foundation to explore the promising capabilities of two-dimensional spectroscopy in the study of nonequilibrium systems. Finally, we see potential in using our approach to investigate disordered magnetic systems and address questions such as the formation of spin glasses, spin liquids, and fractionalized excitations, extending beyond the integrable limit, where most previous works have focused [74, 76, 78, 88, 107, 108].

ACKNOWLEDGEMENTS

We thank R. Andrei, L. Benfatto, U. Bhattacharya, J. Curtis, J. Fiore, A. Malyshev, F. Marijanovic, N. Selati, and E. Vlasiuk for insightful discussions. A.G.S., I.M., and E.D. acknowledge the Swiss National Science Foundation (project 200021.212899) and ETH-C-06 21-2 equilibrium Grant with project number 1-008831-001 for funding. ED acknowledges support from the ARO grant number W911NF-21-1-0184. A.L. was supported by the U.S. Department of Energy, Office of Basic Energy Sciences, under Contract No. DE-SC0012704

Appendix A: Perturbative calculation of $\chi^{(3)}$ to lowest order in g

As a first application of the laid groundwork in Sec. III, we show here an explicit calculation of $\chi^{(3)}$ at first-order in the interaction strength g , i.e., at the tree level:

$$\begin{aligned}
\chi_{\text{mf}}^{(3)}(t_3, t_2, t_1) &= -8i \left\langle \varphi^{\text{cl}}(t_1 + t_2 + t_3) \varphi^q(t_1 + t_2) \varphi^q(t_1) \varphi^q(0) \right. \\
&\quad \times (-i) \int_{-\infty}^{\infty} dt' \int d^d r' \frac{g}{3} \left[\varphi^{\text{cl}}(t', r') (\varphi^q(t', r'))^3 + (\varphi^{\text{cl}}(t', r'))^3 \varphi^q(t', r') \right] \left. \right\rangle \\
&= -g \frac{8}{3} 3! \int_{-\infty}^{\infty} dt' i\mathcal{D}_0^R(t_1 + t_2 + t_3 - t') i\mathcal{D}_0^R(t' - t_1 - t_2) i\mathcal{D}_0^R(t' - t_1) i\mathcal{D}_0^R(t') \\
&= -g \int_{-\infty}^{\infty} dt' \chi^{(1)}(t_1 + t_2 + t_3 - t') \chi^{(1)}(t' - t_1 - t_2) \chi^{(1)}(t' - t_1) \chi^{(1)}(t') \tag{A1}
\end{aligned}$$

and expressed in frequency domain:

$$\chi_{\text{mf}}^{(3)}(\omega_1, \omega_2, \omega_3) \equiv \int dt_1 \int dt_2 \int dt_3 e^{i\omega_1 t_1} e^{i\omega_2 t_2} e^{i\omega_3 t_3} \chi^{(3)}(t_1, t_2, t_3) = -g \chi^{(1)}(\omega_1) \chi^{(1)}(\omega_2 - \omega_1) \chi^{(1)}(\omega_3 - \omega_2) \chi^{(1)}(\omega_3). \tag{A2}$$

Performing the shift in the frequency arguments prescribed in equation (13), $\omega_1 \rightarrow \omega_1$, $\omega_2 \rightarrow \omega_1 + \omega_2$, and $\omega_3 \rightarrow \omega_1 + \omega_2 + \omega_3$ we arrive at

$$\tilde{\chi}_{\text{mf}}^{(3)}(\omega_1, \omega_2, \omega_3) = \chi_{\text{mf}}^{(3)}(\omega_1 + \omega_2 + \omega_3, \omega_1 + \omega_2, \omega_1) = -g \chi^{(1)}(\omega_1) \chi^{(1)}(\omega_2) \chi^{(1)}(\omega_3) \chi^{(1)}(\bar{\omega}), \quad (\text{A3})$$

which provides $\chi^{(3)}$ to the lowest order in g , see Eq. (14) in the main text.

Appendix B: General Structure of $\chi^{(3)}$

In this Appendix we provide a systematic field-theoretical reformulation of the computation of $\chi^{(3)}$ in terms of the effective action. Even though this reformulation is general for arbitrary momentum coupling and measurement, we present it only for the zero momentum scenario in Eq. (B10), which constitutes the central result of this Appendix. At this stage, we redefine for convenience a new source $J^\alpha(\mathbf{r}, t) = 2j^\alpha(\mathbf{r}, t)$, introduce the lumped space-time notation $x = (\mathbf{r}, t)$, and define the one particle irreducible (1PI) effective action as the Legendre transform of $W[J] = i \log Z[J]$, such that:

$$\Xi[\varphi^{\text{cl}}, \varphi^{\text{q}}] = -W[J^{\text{cl}}, J^{\text{q}}] - \int dx \sum_{\alpha} J^{\bar{\alpha}}(x) \phi^{\alpha}(x), \quad (\text{B1})$$

$$\begin{aligned} \frac{\delta W[J]}{\delta J^{\bar{\alpha}}(x)} &= -\langle \varphi^{\alpha}(x; J) \rangle = -\phi^{\alpha}(x; J), \\ \text{and } \frac{\delta \Xi[\phi]}{\delta \phi^{\alpha}(x)} &= -J^{\bar{\alpha}}(x). \end{aligned} \quad (\text{B2})$$

$$\begin{aligned} \frac{\delta^4 W[J]}{\delta J^{\bar{\alpha}_4}(x_4) \delta J^{\bar{\alpha}_3}(x_3) \delta J^{\bar{\alpha}_2}(x_2) \delta J^{\bar{\alpha}_1}(x_1)} &= - \int dt'_1 \int dt'_2 \int dt'_3 \int dt'_4 \sum_{\alpha_1, \alpha_2, \alpha_3, \alpha_4} \Xi^{(4)}(\alpha'_4 x'_4, \alpha'_3 x'_3, \alpha'_2 x'_2, \alpha'_1 x'_1) \\ &\quad \mathcal{D}^{\alpha_4 \alpha'_4}(x_4 - x'_4) \mathcal{D}^{\alpha_3 \alpha'_3}(x_3 - x'_3) \mathcal{D}^{\alpha_2 \alpha'_2}(x_2 - x'_2) \mathcal{D}^{\alpha_1 \alpha'_1}(x_1 - x'_1). \end{aligned} \quad (\text{B6})$$

Here we have employed that $\Xi^{(3)}$ vanishes for the considered system. Hence, the third-order nonlinear response can be computed as

$$\chi^{(3)}(x_3, x_2, x_1) = -8i \frac{\delta^4 W[J]}{\delta J^{\text{q}}(x_3 + x_2 + x_1) \delta J^{\text{cl}}(x_2 + x_1) \delta J^{\text{cl}}(x_1) \delta J^{\text{cl}}(0)}. \quad (\text{B7})$$

Assuming the system has translational invariance, equations (B6) and (B7) can be combined to obtain the convenient expression

$$\tilde{\chi}^{(3)}(p_3, p_2, p_1) = i \Gamma(p_3, p_2, p_1) \prod_i^4 \chi^{(1)}(p_i), \quad (\text{B8})$$

where $p_i = (\mathbf{k}_i, \omega_i)$, $p_4 = (\bar{\mathbf{k}}, \bar{\omega})$, and

$$\Gamma(p_3, p_2, p_1) = \frac{1}{2} \Gamma_{\text{cl}, \text{q}, \text{q}, \text{q}}^{(4)}(\bar{p}, -p_3, -p_2, -p_1). \quad (\text{B9})$$

Here, we have also introduced the convenient notations $\{\bar{\text{cl}}, \bar{\text{q}}\} = \{\text{q}, \text{cl}\}$, and $\int dx = \int d^d \mathbf{r} \int dt$. The effective action fulfils the fundamental relation [84]

$$\begin{aligned} \int dx' \sum_{\gamma} \frac{\delta^2 W[J]}{\delta J^{\bar{\alpha}}(x_1) \delta J^{\bar{\gamma}}(x')} \frac{\delta^2 \Xi[\phi]}{\delta \phi^{\gamma}(x') \delta \phi^{\beta}(x_2)} \\ = \delta_{\bar{\alpha}\bar{\beta}} \delta(x_1 - x_2). \end{aligned} \quad (\text{B3})$$

In particular, this implies that

$$\begin{aligned} \frac{\delta^2 \Xi[\phi]}{\delta \phi^{\alpha}(x_1) \delta \phi^{\beta}(x_2)} &= (\mathcal{D}^{-1})^{\alpha\beta}(x_1 - x_2), \\ \text{since } \frac{\delta^2 W[J]}{\delta J^{\bar{\alpha}}(x_1) \delta J^{\bar{\beta}}(x_2)} &= \mathcal{D}^{\alpha\beta}(x_1 - x_2). \end{aligned} \quad (\text{B4})$$

The n th functional derivative of Ξ

$$\Xi^{(n)}(\alpha_1 x_1, \dots, \alpha_n x_n) = \frac{\delta^n \Xi[\phi]}{\delta \phi^{\alpha_n}(x_n) \dots \delta \phi^{\alpha_1}(x_1)} \quad (\text{B5})$$

is often referred to as the n th 1PI vertex and can be connected to the n th-point connected Green's function. In particular, for the four-point Green's function this relation is given by

Note that in Eq. (B7) we have used that in the Keldysh formalism no vertex containing four external classical legs is possible; this would otherwise lead to a non-vanishing correction to the partition function [85]. For practical purposes when exciting a mode with light, we will be interested in coupling and measuring the zero momentum excitations of the system. Under these assumptions, we set all external momenta to zero and particularize

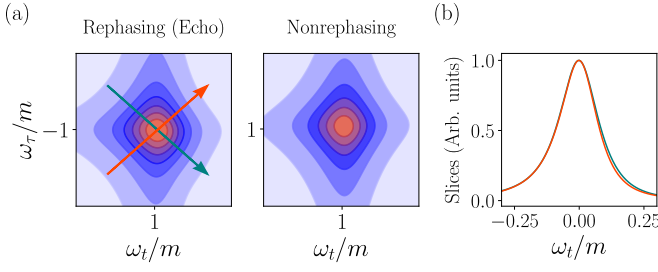


FIG. 10. (a) Echo and nonrephasing peaks in the lowest-order disorder calculation. (b) Slices along the diagonal (teal) and cross-diagonal (orange) of the echo peak. As evident from the peaks itself and the cuts, this approximation is insufficient to capture and characterize the echo peak.

Eq. (B8) to arrive at

$$\tilde{\chi}^{(3)}(\omega_3, \omega_2, \omega_1) = i\Gamma(\omega_3, \omega_2, \omega_1) \prod_i^4 \chi^{(1)}(\omega_i), \quad (\text{B10})$$

c.f. Eq. (16) of the main text.

Appendix C: $\chi^{(3)}$ within the lowest-order disorder approximation

In this Appendix, we briefly discuss the calculation of $\chi^{(3)}$ in the lowest order approximation for the disorder. The employed Luttinger-Ward has the same structure as the one presented in Fig. 6 and is obtained by setting Γ_{dis} to be Γ_{dis}^0 , introduced in Eq. (29). In similar fashion to the discussion of the main text, we compute the self-energy:

$$\begin{aligned} \Sigma_{g-V}^{R(0)}(\omega) &= \text{Diagram 1} + \text{Diagram 2} \\ &= 2 \times \frac{8igV_0^2}{L^{2d}} \sum_{\mathbf{k}, \mathbf{q}} \int \frac{d\Omega}{2\pi} \mathcal{D}_{\mathbf{k}}^R(\omega) \mathcal{D}_{\mathbf{q}-\mathbf{k}}^R(\Omega) \mathcal{D}_{\mathbf{q}}^K(\Omega), \quad (\text{C1}) \end{aligned}$$

the vertex correction

$$\begin{aligned} \text{Diagram 3} &= 2igV_0^2 \left(\frac{4}{L^d} \sum_{\mathbf{k}} \mathcal{D}_{\mathbf{k}}^R(\omega_a) \mathcal{D}_{-\mathbf{k}}^R(\omega_b) \right) \\ &= 2igV_0^2 \lambda(\mathbf{0}; \omega_a, \omega_b) \\ \text{Diagram 4} &= 2igV_0^2 \left(\frac{4}{L^d} \sum_{\mathbf{k}} \mathcal{D}_{\mathbf{k}}^R(\omega_a) \mathcal{D}_{\mathbf{k}}^R(\omega_b) \right) \\ &= 2igV_0^2 \lambda(\mathbf{0}; \omega_a, \omega_b), \quad (\text{C2}) \end{aligned}$$

and the bubble in the presence of disorder:

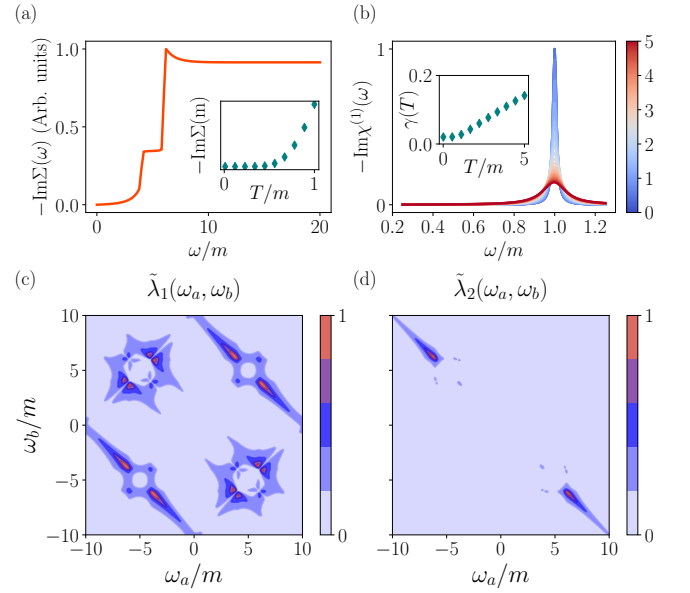


FIG. 11. (a) Imaginary part of the self-energy due to the presence of the optical phonon, for $\mu/m^2 = 1$, $T/m = 1$, and $M/m = 5$. In the inset, the on-shell broadening as a function of temperature. (b) Evolution of the boson linewidth due to the presence of the optical phonon as temperature increases. The inset provides the extracted values of γ after a phenomenological fit to the self-energy. (c)-(d) Color-plot of the absolute value of the tree-level vertex correction for the two distinct vertices (Eqs. (D3) and (D4)) in the presence of the optical phonon; same numerical values as in (a).

$$\begin{aligned} gB_{\text{dis}}^{(0)}(\omega) &= \text{Diagram 5} \\ &= 4igV_0^2 \int \frac{d\Omega}{2\pi} \left(\frac{1}{L^d} \sum_{\mathbf{q}} \mathcal{D}_{\mathbf{q}}^R(\omega + \Omega) \mathcal{D}_{\mathbf{q}}^K(\Omega) \right) \\ &\quad \times \lambda(\mathbf{0}; \omega + \Omega, \Omega). \end{aligned}$$

This concludes the calculation of all the necessary ingredients to compute $\chi^{(3)}$ in the presence of disorder within our conserving approximation. $\chi^{(3)}$ is readily obtained following Eq. (36). We proceed to compute the nonlinear maps, and present the rephasing and nonrephasing peaks in Fig. 10. The echo peak shown in Fig. 10(a) exhibits a slight bludge towards higher energy states, which becomes more apparent when compared to the nonrephasing peak or investigating the slides in Fig. 10(b). This minor asymmetry suggests that the calculation points in the correct direction, but is insufficient to capture the echo peak signature. A more sophisticated treatment, as the one presented in Sec. V, is needed.

Appendix D: Inelastic Scattering

In this Appendix, we present an analogous discussion to Sec. V for the case of inelastic scattering. Diagram-

matically, the analysis requires extra effort because an additional field must be incorporated to model the inelastic scattering events, introducing an additional energy scale, the mass of the mode M . In situations where $M/m \sim 1$, the modes can strongly couple and develop hybridized excitations, leading to a more complicated structure in the 2D map, as expected from the intuition of MDCS [16, 109]. The signatures of hybridization for collective modes in the many-body scenario require careful analysis and are therefore left for future work.

Here, we restrict ourselves to the scenario where the extra mode is an optical phonon with a mass much larger than the one of the collective mode under study, i.e. $M/m \gg 1$. In this regime, the phonon acts as an incoherent bath in which the collective mode can decay, leading to an $i\omega\gamma$ term in its self-energy, where γ characterizes the broadening strength. Furthermore, the phonon can also, in principle, lead to vertex corrections in the four-wave mixing process. Intuitively, the rephasing of the inelastic scattering seems hard to conceive, since the characteristic frequency of the exchanged phonon is $\sim M$, much faster than the typical scale of the boson m . However, as a sanity check, we evaluate the vertex corrections coming from the phonon to confirm that no rephasing is possible. Thus, showing that these corrections can be completely disregarded in the regime $M/m \gg 1$.

The interaction between the collective mode φ and the optical phonon is given by

$$\begin{aligned} S_{ph} &= -\frac{\mu}{2} \int_{\mathcal{C}} dt \int d^d \mathbf{r} \psi(\mathbf{r}, t) \varphi^2(\mathbf{r}, t) \\ &= -\mu \int dt \int d^d \mathbf{r} (\varphi^{\text{cl}} \varphi^{\text{cl}} \psi^{\text{q}} + 2 \varphi^{\text{cl}} \varphi^{\text{q}} \psi^{\text{cl}} + \varphi^{\text{q}} \varphi^{\text{q}} \psi^{\text{q}}), \end{aligned} \quad (\text{D1})$$

where we introduce classical and quantum fields for the phonon analogously to those for the collective mode. Note that, although the coupling structure is similar to that of Eq. (24), key differences arise due to the phonon's dynamics. First, the phonon enables energy transfer to the collective mode. Second, a larger number of diagrams must be considered in both the self-energy and vertex corrections.

1. Self-energy

The lowest order correction to the boson self-energy due to the presence of the optical phonon is given by

$$\begin{aligned} \Sigma^R(\omega) &= \text{Diagram 1} + \text{Diagram 2} = \\ &= \frac{4\mu}{L^d} \sum_{\mathbf{k}} \left(\mathcal{D}_{0\mathbf{k}}^R(\omega) i \tilde{\mathcal{D}}_{0\mathbf{k}}^K(\omega) + i \mathcal{D}_{0\mathbf{k}}^K(\omega) \tilde{\mathcal{D}}_{0\mathbf{k}}^R(\omega) \right) \end{aligned} \quad (\text{D2})$$

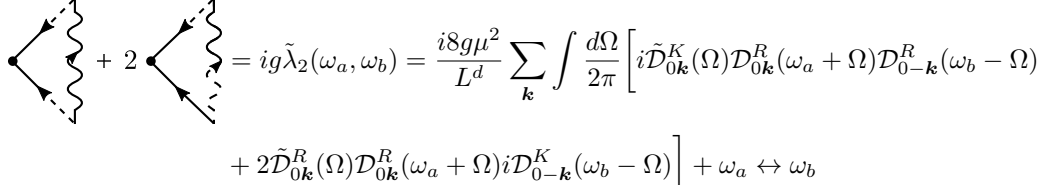
where $2\tilde{\mathcal{D}}_{\mathbf{k}}^R(\omega) = ((\omega + i\eta)^2 - M^2)^{-1}$ is the phonon retarded Green's function at momentum \mathbf{k} and frequency ω . To keep the mass of the excitation fixed at the physical mass m , we introduce a mass counterterm $\delta_m = \text{Re}\{\Sigma(\omega = m)\}$, such that $m^2 = m_0^2 + \text{Re}\Sigma(m) - \delta_m$. Since the phonon can now exchange energy with the excitation of interest, the fluctuations of the phonon field control the linewidth broadening. At small temperatures, the phonon fluctuations are exponentially suppressed, and the broadening is negligible. Upon increasing temperature, the phonon fluctuations become sizable, resulting in a broadening of the boson linewidth, as can be seen in Fig. 11 (a) and (b). This is a generic feature that can be phenomenologically captured, independently of the coupling strength μ or mass M , by a self-energy term of the form $i\omega\gamma(T)$, where γ characterizes the broadening of the linewidth.

2. Vertices

Similarly to the case of elastic scattering, we evaluate the vertex corrections in the presence of the phonon. Here, we compute the vertices only to lowest order to demonstrate that, in the limit $M/m \gg 1$, they can be completely disregarded. Unlike for the case of elastic scattering, Eq. (34), the vertices cannot be reexpressed as a single vertex and have to be computed independently. These correspond to the exchange of a phonon between two incoming, or one incoming and one outgoing bosons and are given by

$$\begin{aligned} \text{Diagram 1} + \text{Diagram 2} + \text{Diagram 3} &= ig\tilde{\lambda}_1(\omega_a, \omega_b) = \frac{i8g\mu^2}{L^d} \sum_{0\mathbf{k}} \int \frac{d\Omega}{2\pi} \left[i \tilde{\mathcal{D}}_{0\mathbf{k}}^K(\Omega) \mathcal{D}_{0\mathbf{k}}^R(\omega_a + \Omega) \mathcal{D}_{0\mathbf{k}}^R(\omega_b + \Omega) \right. \\ &\quad \left. + \tilde{\mathcal{D}}_{0-\mathbf{k}}^R(-\Omega) \mathcal{D}_{0\mathbf{k}}^R(\omega_a + \Omega) i \mathcal{D}_{0\mathbf{k}}^K(\omega_b + \Omega) + \tilde{\mathcal{D}}_{0\mathbf{k}}^R(\Omega) \mathcal{D}_{0\mathbf{k}}^R(\omega_a + \Omega) i \mathcal{D}_{0\mathbf{k}}^K(\omega_b + \Omega) \right] + \omega_a \leftrightarrow \omega_b \end{aligned} \quad (\text{D3})$$

and



$$\begin{aligned}
 & \text{Diagram 1} + 2 \text{Diagram 2} = ig\tilde{\lambda}_2(\omega_a, \omega_b) = \frac{i8g\mu^2}{L^d} \sum_{\mathbf{k}} \int \frac{d\Omega}{2\pi} \left[i\tilde{\mathcal{D}}_{0\mathbf{k}}^K(\Omega) \mathcal{D}_{0\mathbf{k}}^R(\omega_a + \Omega) \mathcal{D}_{0-\mathbf{k}}^R(\omega_b - \Omega) \right. \\
 & \left. + 2\tilde{\mathcal{D}}_{0\mathbf{k}}^R(\Omega) \mathcal{D}_{0\mathbf{k}}^R(\omega_a + \Omega) i\mathcal{D}_{0-\mathbf{k}}^K(\omega_b - \Omega) \right] + \omega_a \leftrightarrow \omega_b \quad (\text{D4})
 \end{aligned}$$

To show that there is no rephasing physics involved in these vertex corrections for $M/m \gg 1$, we present a color-plot of the absolute value of the two vertices $\tilde{\lambda}_1$ and $\tilde{\lambda}_2$ in Fig. 11(c) and (d) for $M/m = 5$. Indeed, the fast dynamics of the phonon $\sim M$ push the effects of the vertex corrections to $\omega_a \sim \omega_b \sim M$, resulting in a negligible contribution in the frequency region of the boson mass m . However, as aforementioned, for $M/m \sim 1$ the vertex corrections can be important around the mass energy m and may give rise to interesting signatures in the

2D map.

As a last comment, we note that from the phonon-boson action in Eq. (D1) an effective vertex with external legs $cl-cl-cl-q$ arises, which contributes to the nonlinear response. However, the effective interaction scales as $\sim \mu^2/M^2$, for a large phononic mass. Therefore, we can safely ignore its corrections to the preexisting interaction strength g .

-
- [1] A. Guinier, *X-ray diffraction in crystals, imperfect crystals, and amorphous bodies* (Courier Corporation, 1994).
- [2] R. Comin and A. Damascelli, Resonant x-ray scattering studies of charge order in cuprates, *Annual Review of Condensed Matter Physics* **7**, 369 (2016).
- [3] J. Jimenez and J. W. Tomm, Basics of optical spectroscopy: Transmission and reflection measurements, their analysis, and related techniques, in *Spectroscopic Analysis of Optoelectronic Semiconductors* (Springer International Publishing, Cham, 2016) pp. 49–76.
- [4] R. Robson, R. White, and M. Hildebrandt, *Fundamentals of Charged Particle Transport in Gases and Condensed Matter* (CRC Press, 2017).
- [5] J. P. Pekola and B. Karimi, Colloquium: Quantum heat transport in condensed matter systems, *Rev. Mod. Phys.* **93**, 041001 (2021).
- [6] G. Binnig and H. Rohrer, Scanning tunneling microscopy—from birth to adolescence, *Rev. Mod. Phys.* **59**, 615 (1987).
- [7] A. Damascelli, Z. Hussain, and Z.-X. Shen, Angle-resolved photoemission studies of the cuprate superconductors, *Rev. Mod. Phys.* **75**, 473 (2003).
- [8] R. Ernst, G. Bodenhausen, and A. Wokaun, *Principles of Nuclear Magnetic Resonance in One and Two Dimensions*, International series of monographs on chemistry (Clarendon Press, 1990).
- [9] H. Friebolin, *Basic One- and Two-dimensional NMR Spectroscopy* (VCH, 1991).
- [10] O. Zerbe and H. Jurt, *Applied NMR Spectroscopy for Chemists and Life Scientists* (Wiley VCH, 2013).
- [11] B. Reif, S. E. Ashbrook, L. Emsley, and M. Hong, Solid-state nmr spectroscopy, *Nature Reviews Methods Primers* **1**, 2 (2021).
- [12] D. McRobbie, E. Moore, M. Graves, and M. Prince, *MRI from Picture to Proton* (Cambridge University Press, 2017).
- [13] H. K. Kim, Y. H. Choi, and R. Verpoorte, Nmr-based metabolomic analysis of plants, *Nature Protocols* **5**, 536 (2010).
- [14] J. Keeler, *Understanding NMR spectroscopy* (John Wiley & Sons, 2010).
- [15] S. Mukamel, *Principles of Nonlinear Optical Spectroscopy*, Oxford series in optical and imaging sciences (Oxford University Press, 1995).
- [16] P. Hamm and M. Zanni, *Concepts and Methods of 2D Infrared Spectroscopy* (Cambridge University Press, 2011).
- [17] S. T. Cundiff and S. Mukamel, Optical multidimensional coherent spectroscopy, *Physics Today* **66**, 44 (2013).
- [18] L. Bruder, U. Bangert, M. Binz, D. Uhl, and F. Stienke-meier, Coherent multidimensional spectroscopy in the gas phase, *Journal of Physics B: Atomic, Molecular and Optical Physics* **52**, 183501 (2019).
- [19] S. Mukamel, Y. Tanimura, and P. Hamm, Coherent multidimensional optical spectroscopy, *Accounts of Chemical Research* **42**, 1207 (2009).
- [20] M. K. Petti, J. P. Lomont, M. Maj, and M. T. Zanni, Two-dimensional spectroscopy is being used to address core scientific questions in biology and materials science, *The Journal of Physical Chemistry B* **122**, 1771 (2018).
- [21] S. T. Cundiff, Optical two-dimensional fourier transform spectroscopy of semiconductor nanostructures [invited], *Journal of the Optical Society of America B* **29**, A69 (2012).
- [22] E. Fresch, F. Camargo, Q. Shen, C. Bellora, T. Pullerits, G. Engel, G. Cerullo, and E. Collini, Two-dimensional electronic spectroscopy, *Nature Reviews Methods Primers* **3**, 10.1038/s43586-023-00267-2 (2023).
- [23] B. Lomsadze and S. T. Cundiff, Frequency combs enable rapid and high-resolution multidimensional coherent

- ent spectroscopy, *Science* **357**, 1389 (2017).
- [24] A. Liu, D. B. Almeida, W. K. Bae, L. A. Padilha, and S. T. Cundiff, Non-markovian exciton-phonon interactions in core-shell colloidal quantum dots at femtosecond timescales, *Phys. Rev. Lett.* **123**, 057403 (2019).
- [25] J. B. Muir, J. Levinsen, S. K. Earl, M. A. Conway, J. H. Cole, M. Wurdack, R. Mishra, D. J. Ing, E. Estrecho, Y. Lu, D. K. Efimkin, J. O. Tollerud, E. A. Ostrovskaya, M. M. Parish, and J. A. Davis, Interactions between fermi polarons in monolayer ws_2 , *Nature Communications* **13**, 6164 (2022).
- [26] R. Singh, G. Moody, M. E. Siemens, H. Li, and S. T. Cundiff, Quantifying spectral diffusion by the direct measurement of the correlation function for excitons in semiconductor quantum wells, *J. Opt. Soc. Am. B* **33**, C137 (2016).
- [27] J. D. Hybl, A. W. Albrecht, S. M. Gallagher Faeder, and D. M. Jonas, Two-dimensional electronic spectroscopy, *Chemical Physics Letters* **297**, 307 (1998).
- [28] G. S. Engel, T. R. Calhoun, E. L. Read, T.-K. Ahn, T. Mančal, Y.-C. Cheng, R. E. Blankenship, and G. R. Fleming, Evidence for wavelike energy transfer through quantum coherence in photosynthetic systems, *Nature* **446**, 782 (2007).
- [29] C. L. Johnson, B. E. Knighton, and J. A. Johnson, Distinguishing nonlinear terahertz excitation pathways with two-dimensional spectroscopy, *Phys. Rev. Lett.* **122**, 073901 (2019).
- [30] K. W. Stone, K. Gundogdu, D. B. Turner, X. Li, S. T. Cundiff, and K. A. Nelson, Two-quantum 2d ft electronic spectroscopy of biexcitons in gaas quantum wells, *Science* **324**, 1169 (2009).
- [31] K. Hao, L. Xu, F. Wu, P. Nagler, K. Tran, X. Ma, C. Schüller, T. Korn, A. H. MacDonald, G. Moody, *et al.*, Trion valley coherence in monolayer semiconductors, *2D Materials* **4**, 025105 (2017).
- [32] K. Hao, J. F. Specht, P. Nagler, L. Xu, K. Tran, A. Singh, C. K. Dass, C. Schüller, T. Korn, M. Richter, A. Knorr, X. Li, and G. Moody, Neutral and charged inter-valley biexcitons in monolayer mose_2 , *Nature Communications* **8**, 15552 (2017).
- [33] A. Bristow, T. Zhang, M. Siemens, S. Cundiff, and R. Mirin, Separating homogeneous and inhomogeneous line widths of heavy- and light-hole excitons in weakly disordered semiconductor quantum wells, *The Journal of Physical Chemistry B* **115**, 5365–5371 (2011).
- [34] G. Moody, C. Kavir Dass, K. Hao, C.-H. Chen, L.-J. Li, A. Singh, K. Tran, G. Clark, X. Xu, G. Berghäuser, E. Malic, A. Knorr, and X. Li, Intrinsic homogeneous linewidth and broadening mechanisms of excitons in monolayer transition metal dichalcogenides, *Nature Communications* **6**, 8315 (2015).
- [35] D. Huang, K. Sampson, Y. Ni, Z. Liu, D. Liang, K. Watanabe, T. Taniguchi, H. Li, E. Martin, J. Levinsen, M. M. Parish, E. Tutuc, D. K. Efimkin, and X. Li, Quantum dynamics of attractive and repulsive polarons in a doped mose_2 monolayer, *Phys. Rev. X* **13**, 011029 (2023).
- [36] M. H. Michael, A. von Hoegen, M. Fechner, M. Först, A. Cavalleri, and E. Demler, Parametric resonance of josephson plasma waves: A theory for optically amplified interlayer superconductivity in $\text{yba}_2\text{cu}_3\text{o}_{6+x}$, *Phys. Rev. B* **102**, 174505 (2020).
- [37] N. Sellati, F. Gabriele, C. Castellani, and L. Benfatto, Generalized josephson plasmons in bilayer superconductors, *Phys. Rev. B* **108**, 014503 (2023).
- [38] J. Fiore, N. Sellati, F. Gabriele, C. Castellani, G. Seibold, M. Udina, and L. Benfatto, Investigating josephson plasmons in layered cuprates via nonlinear terahertz spectroscopy, *Phys. Rev. B* **110**, L060504 (2024).
- [39] N. Sellati, J. Fiore, C. Castellani, and L. Benfatto, Optical absorption in tilted geometries as an indirect measurement of longitudinal plasma waves in layered cuprates, *Nanomaterials* **14**, 10.3390/nano14121021 (2024).
- [40] N. Taherian, M. Först, A. Liu, M. Fechner, D. Pavicevic, A. von Hoegen, E. Rowe, Y. Liu, S. Nakata, B. Keimer, E. Demler, M. H. Michael, and A. Cavalleri, Squeezed josephson plasmons in driven $\text{YBa}_2\text{Cu}_3\text{O}_{6+x}$ (2024), arXiv:2401.01115 [cond-mat.supr-con].
- [41] M.-J. Kim, S. Kovalev, M. Udina, R. Haenel, G. Kim, M. Puviani, G. Cristiani, I. Ilyakov, T. V. A. G. de Oliveira, A. Ponomaryov, J.-C. Deinert, G. Logvenov, B. Keimer, D. Manske, L. Benfatto, and S. Kaiser, Tracing the dynamics of superconducting order via transient terahertz third-harmonic generation, *Science Advances* **10**, eadi7598 (2024), <https://www.science.org/doi/pdf/10.1126/sciadv.adi7598>.
- [42] K. Zakeri, Terahertz magnonics: Feasibility of using terahertz magnons for information processing, *Physica C: Superconductivity and its Applications* **549**, 164 (2018).
- [43] L. Peedu, V. Kocsis, D. Szaller, B. Forrai, S. Bordács, I. Kézsmárki, J. Viirok, U. Nagel, B. Bernáth, D. L. Kamenskyi, A. Miyata, O. Portugall, Y. Tokunaga, Y. Tokura, Y. Taguchi, and T. Rõ om, Terahertz spectroscopy of spin excitations in magnetoelectric lifepo_4 in high magnetic fields, *Phys. Rev. B* **106**, 134413 (2022).
- [44] B. S. Mehra, S. Kumar, G. Dubey, A. Shyam, A. Kumar, K. Anirudh, K. Singh, and D. S. Rana, Myriad of terahertz magnons with all-optical magnetoelectric functionality for efficient spin-wave computing in honeycomb magnet $\text{co}_4\text{ta}_2\text{o}_9$ (2024), arXiv:2407.00597 [cond-mat.mtrl-sci].
- [45] J. Lloyd-Hughes, Terahertz spectroscopy of quantum 2d electron systems, *Journal of Physics D: Applied Physics* **47**, 374006 (2014).
- [46] G. Scalari, C. Maissen, D. Turčinková, D. Hagenmüller, S. D. Liberato, C. Ciuti, C. Reichl, D. Schuh, W. Wegscheider, M. Beck, and J. Faist, Ultrastrong coupling of the cyclotron transition of a 2d electron gas to a thz metamaterial, *Science* **335**, 1323 (2012).
- [47] D. Pavlidis, *Fundamentals of Terahertz Devices and Applications* (Wiley VCH, 2021).
- [48] D. Nicoletti and A. Cavalleri, Nonlinear light-matter interaction at terahertz frequencies, *Advances in Optics and Photonics* **8**, 401 (2016).
- [49] J. A. Fülöp, S. Tzortzakis, and T. Kampfrath, Laser-driven strong-field terahertz sources, *Advanced Optical Materials* **8**, 1900681 (2020).
- [50] J. Lu, Y. Zhang, H. Y. Hwang, B. K. Ofori-Okai, S. Fleischer, and K. A. Nelson, Nonlinear two-dimensional terahertz photon echo and rotational spectroscopy in the gas phase, *Proceedings of the National Academy of Sciences* **113**, 11800 (2016), <https://www.pnas.org/doi/pdf/10.1073/pnas.1609558113>.
- [51] T. Maag, A. Bayer, S. Baierl, M. Hohenleutner, T. Korn, C. Schüller, D. Schuh, D. Bougeard, C. Lange, R. Huber, M. Mootz, J. E. Sipe, S. W. Koch, and

- M. Kira, Coherent cyclotron motion beyond Kohn's theorem, *Nature Physics* **12**, 119 (2016).
- [52] S. Houver, L. Huber, M. Savoini, E. Abreu, and S. L. Johnson, 2d thz spectroscopic investigation of ballistic conduction-band electron dynamics in insb, *Opt. Express* **27**, 10854 (2019).
- [53] F. Mahmood, D. Chaudhuri, S. Gopalakrishnan, R. Nandkishore, and N. P. Armitage, Observation of a marginal Fermi glass, *Nature Physics* **17**, 627 (2021).
- [54] S. Pal, N. Strkalj, C.-J. Yang, M. C. Weber, M. Trassin, M. Woerner, and M. Fiebig, Origin of terahertz soft-mode nonlinearities in ferroelectric perovskites, *Phys. Rev. X* **11**, 021023 (2021).
- [55] H.-W. Lin, G. Mead, and G. A. Blake, Mapping linbo₃ phonon-polariton nonlinearities with 2d thz-thz-raman spectroscopy, *Phys. Rev. Lett.* **129**, 207401 (2022).
- [56] L. Luo, M. Mootz, J. H. Kang, C. Huang, K. Eom, J. W. Lee, C. Vaswani, Y. G. Collantes, E. E. Hellstrom, I. E. Perakis, C. B. Eom, and J. Wang, Quantum coherence tomography of light-controlled superconductivity, *Nature Physics* **19**, 201 (2023).
- [57] K. Reimann, M. Woerner, and T. Elsaesser, Two-dimensional terahertz spectroscopy of condensed-phase molecular systems, *The Journal of Chemical Physics* **154**, 120901 (2021).
- [58] A. Liu, D. Pavićević, M. H. Michael, A. G. Salvador, P. E. Dolgirev, M. Fechner, A. S. Disa, P. M. Lozano, Q. Li, G. D. Gu, E. Demler, and A. Cavalleri, Probing inhomogeneous cuprate superconductivity by terahertz josephson echo spectroscopy, *Nature Physics* **20**, 1751 (2024).
- [59] A. Liu, *Multidimensional terahertz probes of quantum materials* (2024), arXiv:2409.03719 [cond-mat.mtrl-sci].
- [60] D. Soranzio, E. Abreu, S. Houver, J. Dössegger, M. Savoini, F. Teppe, S. Krishtopenko, N. N. Mikhailov, S. A. Dvoretzky, and S. L. Johnson, Roles of band gap and kane electronic dispersion in the terahertz-frequency nonlinear optical response in hgcdte, *Phys. Rev. B* **110**, 094303 (2024).
- [61] A. Liu and A. Disa, Excitation-dependent features and artifacts in 2-d terahertz spectroscopy, *Opt. Express* **32**, 28160 (2024).
- [62] M. Mootz, L. Luo, J. Wang, and I. E. Perakis, Visualization and quantum control of light-accelerated condensates by terahertz multi-dimensional coherent spectroscopy, *Communications Physics* **5**, 47 (2022).
- [63] M. Puviani and D. Manske, Quench-drive spectroscopy of cuprates, *Faraday Discuss.* **237**, 125 (2022).
- [64] M. Puviani, R. Haenel, and D. Manske, Quench-drive spectroscopy and high-harmonic generation in bcs superconductors, *Phys. Rev. B* **107**, 094501 (2023).
- [65] K. Katsumi, J. Fiore, M. Udina, R. Romero, D. Barbalas, J. Jesudasan, P. Raychaudhuri, G. Seibold, L. Benfatto, and N. P. Armitage, Revealing novel aspects of light-matter coupling by terahertz two-dimensional coherent spectroscopy: The case of the amplitude mode in superconductors, *Phys. Rev. Lett.* **132**, 256903 (2024).
- [66] M. Puviani, Theory of symmetry-resolved quench-drive spectroscopy: Nonlinear response of phase-fluctuating superconductors, *Phys. Rev. B* **109**, 214515 (2024).
- [67] K. Katsumi, J. Liang, R. R. I. au2, K. Chen, X. Xi, and N. P. Armitage, Amplitude mode in a multi-gap superconductor mgb₂ investigated by terahertz two-dimensional coherent spectroscopy (2024), arXiv:2411.10852 [cond-mat.supr-con].
- [68] D. Barbalas, R. Romero, D. Chaudhuri, F. Mahmood, H. P. Nair, N. J. Schreiber, D. G. Schlom, K. M. Shen, and N. P. Armitage, Energy relaxation and dynamics in the correlated metal sr₂ruo₄ via terahertz two-dimensional coherent spectroscopy, *Phys. Rev. Lett.* **134**, 036501 (2025).
- [69] J. Chen and P. Werner, Multidimensional coherent spectroscopy of correlated lattice systems (2024), arXiv:2411.02389 [cond-mat.str-el].
- [70] J. Lu, X. Li, H. Y. Hwang, B. K. Ofori-Okai, T. Kurihara, T. Suemoto, and K. A. Nelson, Coherent two-dimensional terahertz magnetic resonance spectroscopy of collective spin waves, *Phys. Rev. Lett.* **118**, 207204 (2017).
- [71] H.-W. Lin, G. Mead, and G. A. Blake, Mapping linbo₃ phonon-polariton nonlinearities with 2d thz-thz-raman spectroscopy, *Phys. Rev. Lett.* **129**, 207401 (2022).
- [72] Z. Zhang, F. Y. Gao, Y.-C. Chien, Z.-J. Liu, J. B. Curtis, E. R. Sung, X. Ma, W. Ren, S. Cao, P. Narang, A. von Hoegen, E. Baldini, and K. A. Nelson, Terahertz-field-driven magnon upconversion in an antiferromagnet, *Nature Physics* **20**, 788 (2024).
- [73] Z. Zhang, F. Y. Gao, J. B. Curtis, Z.-J. Liu, Y.-C. Chien, A. von Hoegen, M. T. Wong, T. Kurihara, T. Suemoto, P. Narang, E. Baldini, and K. A. Nelson, Terahertz field-induced nonlinear coupling of two magnon modes in an antiferromagnet, *Nature Physics* **20**, 801 (2024).
- [74] S. A. Parameswaran and S. Gopalakrishnan, Asymptotically exact theory for nonlinear spectroscopy of random quantum magnets, *Phys. Rev. Lett.* **125**, 237601 (2020).
- [75] T. G. H. Blank, K. A. Grishunin, K. A. Zvezdin, N. T. Hai, J. C. Wu, S.-H. Su, J.-C. A. Huang, A. K. Zvezdin, and A. V. Kimel, Two-dimensional terahertz spectroscopy of nonlinear phononics in the topological insulator mnbi₂te₄, *Phys. Rev. Lett.* **131**, 026902 (2023).
- [76] Y. Wan and N. P. Armitage, Resolving continua of fractional excitations by spinon echo in thz 2d coherent spectroscopy, *Phys. Rev. Lett.* **122**, 257401 (2019).
- [77] O. Liebman, J. Curtis, I. Petrides, and P. Narang, Multiphoton spectroscopy of a dynamical axion insulator (2023), arXiv:2306.00064 [cond-mat.str-el].
- [78] W. Choi, K. H. Lee, and Y. B. Kim, Theory of two-dimensional nonlinear spectroscopy for the kitaev spin liquid, *Phys. Rev. Lett.* **124**, 117205 (2020).
- [79] M. McGinley, M. Fava, and S. A. Parameswaran, Signatures of fractional statistics in nonlinear pump-probe spectroscopy, *Phys. Rev. Lett.* **132**, 066702 (2024).
- [80] M. McGinley, M. Fava, and S. A. Parameswaran, Anomalous thermal relaxation and pump-probe spectroscopy of two-dimensional topologically ordered systems, *Phys. Rev. B* **109**, 075108 (2024).
- [81] M. Potts, R. Moessner, and O. Benton, Signatures of spinon dynamics and phase structure of dipolar-octupolar quantum spin ices in two-dimensional coherent spectroscopy (2024), arXiv:2406.01472 [cond-mat.str-el].
- [82] E. L. Hahn, Spin echoes, *Phys. Rev.* **80**, 580 (1950).
- [83] M. E. Siemens, G. Moody, H. Li, A. D. Bristow, and S. T. Cundiff, Resonance lineshapes in two-dimensional fourier transform spectroscopy, *Opt. Express* **18**, 17699

- (2010).
- [84] N. Dupuis, *Field Theory Of Condensed Matter And Ultracold Gases-Volume 1* (World Scientific, 2023).
- [85] A. Kamenev, *Field theory of non-equilibrium systems* (Cambridge University Press, 2023).
- [86] M. E. Peskin, *An introduction to quantum field theory* (CRC press, 2018).
- [87] J. Berges, Introduction to nonequilibrium quantum field theory, in *AIP Conference Proceedings*, Vol. 739 (American Institute of Physics, 2004) pp. 3–62.
- [88] O. Hart and R. Nandkishore, Extracting spinon self-energies from two-dimensional coherent spectroscopy, *Phys. Rev. B* **107**, 205143 (2023).
- [89] A. G. Salvador, P. E. Dolgirev, M. H. Michael, A. Liu, D. Pavicevic, M. Fechner, A. Cavalleri, and E. Demler, Principles of 2d terahertz spectroscopy of collective excitations: the case of josephson plasmons in layered superconductors (2024), arXiv:2401.05503 [cond-mat.supr-con].
- [90] G. Baym and L. P. Kadanoff, Conservation laws and correlation functions, *Phys. Rev.* **124**, 287 (1961).
- [91] G. Baym, Self-consistent approximations in many-body systems, *Phys. Rev.* **127**, 1391 (1962).
- [92] C. Wetterich, Exact evolution equation for the effective potential, *Physics Letters B* **301**, 90 (1993).
- [93] J. Berges, N. Tetradis, and C. Wetterich, Non-perturbative renormalization flow in quantum field theory and statistical physics, *Physics Reports* **363**, 223 (2002), renormalization group theory in the new millennium. IV.
- [94] N. Dupuis, L. Canet, A. Eichhorn, W. Metzner, J. Pawłowski, M. Tissier, and N. Wschebor, The non-perturbative functional renormalization group and its applications, *Physics Reports* **910**, 1 (2021), the non-perturbative functional renormalization group and its applications.
- [95] L. N. Bulaevskii, M. Zamora, D. Baeriswyl, H. Beck, and J. R. Clem, Time-dependent equations for phase differences and a collective mode in josephson-coupled layered superconductors, *Phys. Rev. B* **50**, 12831 (1994).
- [96] M. V. Sadovskii, *Diagrammatics: lectures on selected problems in condensed matter theory* (World Scientific, 2006).
- [97] E. Akkermans and G. Montambaux, *Mesoscopic physics of electrons and photons* (Cambridge university press, 2007).
- [98] J. Billy, V. Josse, Z. Zuo, A. Bernard, B. Hambrecht, P. Lugan, D. Clément, L. Sanchez-Palencia, P. Bouyer, and A. Aspect, Direct observation of anderson localization of matter waves in a controlled disorder, *Nature* **453**, 891 (2008).
- [99] G. Roati, C. D’Errico, L. Fallani, M. Fattori, C. Fort, M. Zaccanti, G. Modugno, M. Modugno, and M. Inguscio, Anderson localization of a non-interacting bose-einstein condensate, *Nature* **453**, 895 (2008).
- [100] E. C. Fulmer, F. Ding, P. Mukherjee, and M. T. Zanni, Vibrational dynamics of ions in glass from fifth-order two-dimensional infrared spectroscopy, *Phys. Rev. Lett.* **94**, 067402 (2005).
- [101] A. de la Torre, D. M. Kennes, M. Claassen, S. Gerber, J. W. McIver, and M. A. Sentef, Colloquium: Nonthermal pathways to ultrafast control in quantum materials, *Rev. Mod. Phys.* **93**, 041002 (2021).
- [102] X. Li, T. Qiu, J. Zhang, E. Baldini, J. Lu, A. M. Rappe, and K. A. Nelson, Terahertz field-induced ferroelectricity in quantum paraelectric SrTiO_3 , *Science* **364**, 1079 (2019), <https://www.science.org/doi/pdf/10.1126/science.aaw4913>.
- [103] T. F. Nova, A. S. Disa, M. Fechner, and A. Cavalleri, Metastable ferroelectricity in optically strained SrTiO_3 , *Science* **364**, 1075 (2019), <https://www.science.org/doi/pdf/10.1126/science.aaw4911>.
- [104] D. Fausti, R. I. Tobey, N. Dean, S. Kaiser, A. Dienst, M. C. Hoffmann, S. Pyon, T. Takayama, H. Takagi, and A. Cavalleri, Light-induced superconductivity in a stripe-ordered cuprate, *Science* **331**, 189 (2011), <https://www.science.org/doi/pdf/10.1126/science.1197294>.
- [105] M. Mitrano, A. Cantaluppi, D. Nicoletti, S. Kaiser, A. Perucchi, S. Lupi, P. Di Pietro, D. Pontiroli, M. Riccò, S. R. Clark, D. Jaksch, and A. Cavalleri, Possible light-induced superconductivity in $\text{K}_3\text{C}_6\text{O}$ at high temperature, *Nature* **530**, 461 (2016).
- [106] S. Fava, G. De Vecchi, G. Jotzu, M. Buzzi, T. Gebert, Y. Liu, B. Keimer, and A. Cavalleri, Magnetic field expulsion in optically driven $\text{YBa}_2\text{Cu}_3\text{O}_{6.48}$, *Nature* **632**, 75 (2024).
- [107] M. Fava, S. Gopalakrishnan, R. Vasseur, F. Essler, and S. A. Parameswaran, Divergent nonlinear response from quasiparticle interactions, *Phys. Rev. Lett.* **131**, 256505 (2023).
- [108] M. Fava, S. Gopalakrishnan, R. Vasseur, S. A. Parameswaran, and F. H. L. Essler, Long-time divergences in the nonlinear response of gapped one-dimensional many-particle systems (2024), arXiv:2411.06167 [cond-mat.str-el].
- [109] J. Edler and P. Hamm, Two-dimensional vibrational spectroscopy of the amide I band of crystalline acetanilide: Fermi resonance, conformational substates, or vibrational self-trapping?, *The Journal of Chemical Physics* **119**, 2709 (2003), https://pubs.aip.org/aip/jcp/article-pdf/119/5/2709/19321607/2709_1_online.pdf.